The Astrophysical Journal, 998:255 (28pp), 2026 February 20 https://doi.org/10.3847/1538-4357/ae32f1

Protoplanetary Disk Cavities with JWST-MIRI: A Dichotomy in Molecular Emission

Patrick Mallaney[1,19], Andrea Banzatti[1,19], Colette Salyk[2], Ilaria Pascucci[3], Paola Pinilla[4], Joan Najita[5], Klaus M. Pontoppidan[6], Sebastiaan Krijt[7], Geoffrey A. Blake[8], Benoît Tabone[9], Till Kaeufer[7], Ke Zhang[10], Feng Long[3,20], Jane Huang[11], Giovanni Rosotti[12], Karin I. Öberg[13], María José Colmenares[14], Andrew Lay[1], Lucas A. Cieza[15], L. Ilsedore Cleeves[16], Joe Williams[7], Chengyan Xie[3], Miguel Vioque[17], Mayank Narang[6], Nicholas P. Ballering[18], Minjae Kim[4], and The JDISCS Collaboration
[1] Department of Physics, Texas State University, 749 N Comanche Street, San Marcos, TX 78666, USA; pmallane@nd.edu, banzatti@txstate.edu
[2] Department of Physics and Astronomy, Vassar College, 124 Raymond Avenue, Poughkeepsie, NY 12604, USA
[3] Department of Planetary Sciences, University of Arizona, 1629 East University Boulevard, Tucson, AZ 85721, USA
[4] Mullard Space Science Laboratory, University College London, Holmbury St Mary, Dorking, Surrey RH5 6NT, UK
[5] NSF's NOIRLab, 950 N. Cherry Avenue, Tucson, AZ 85719, USA
[6] Jet Propulsion Laboratory, California Institute of Technology, 4800 Oak Grove Drive, Pasadena, CA 91109, USA
[7] School of Physics and Astronomy, University of Exeter, Stocker Road, Exeter EX4 4QL, UK
[8] Division of Geological & Planetary Sciences, MC 150-21, California Institute of Technology, Pasadena, CA 91125, USA
[9] Université Paris-Saclay, CNRS, Institut d'Astrophysique Spatiale, 91405 Orsay, France
[10] Department of Astronomy, University of Wisconsin-Madison, Madison, WI 53706, USA
[11] Department of Astronomy, Columbia University, 538 W. 120th Street, Pupin Hall, New York, NY 10027, USA
[12] Dipartimento di Fisica, Università degli Studi di Milano, via Giovanni Celoria 16, 20133, Milano, Italy
[13] Center for Astrophysics, Harvard & Smithsonian, 60 Garden Street, Cambridge, MA 02138, USA
[14] Department of Astronomy, University of Michigan, Ann Arbor, MI 48109, USA
[15] Núcleo de Astronomía, Facultad de Ingeniería y Ciencias, Universidad Diego Portales, Av Ejército 441, Santiago, Chile
[16] Astronomy Department, University of Virginia, Charlottesville, VA 22904, USA
[17] European Southern Observatory, Karl-Schwarzschild-Str. 2, 85748, Garching bei München, Germany
[18] Space Science Institute, Boulder, CO 80301, USA
Received 2025 August 27; revised 2025 December 29; accepted 2025 December 30; published 2026 February 13

Abstract

The evolution of planet-forming regions in protoplanetary disks is of fundamental importance to understanding planet formation. Disks with a central deficit in dust emission, a "cavity," have long attracted interest as potential evidence for advanced disk clearing by protoplanets and/or winds. Before JWST, infrared spectra showed that these disks typically lack the strong molecular emission observed in full disks. In this work, we combine a sample of 12 disks with millimeter cavities of a range of sizes (∼2–70 au) and different levels of millimeter and infrared continuum deficits. We analyze their molecular spectra as observed with MIRI on JWST, homogeneously reduced with the new JDISCS pipeline. This analysis demonstrates a stark dichotomy in molecular emission where "molecule-rich" (MR) cavities follow global trends between water, CO, and OH luminosity and accretion luminosity as in full disks, while "molecule-poor" (MP) cavities are significantly subluminous in all molecules except sometimes OH. Disk cavities generally show subluminous organic emission, higher OH/H_2O ratios, and suggest a lower water column density. The subthermal excitation of CO and water vibrational lines suggests a decreased gas density in the emitting layer in all cavities, supporting model expectations for C_2H_2 photodissociation. We discover a bifurcation in the infrared index (lower in MR cavities) suggesting that the molecular dichotomy is linked to residual μm-size dust within millimeter disk cavities. Put together, these results suggest a feedback process between dust depletion, gas density decrease, and molecule dissociation. Disk cavities may have a common evolutionary sequence where MR switch into MP over time.

Unified Astronomy Thesaurus concepts: Protoplanetary disks (1300); Exoplanet formation (492); Molecular spectroscopy (2095); Infrared spectroscopy (2285); Young stellar objects (1834); T Tauri stars (1681); Circumstellar disks (235); Planet formation (1241); Star formation (1569); Pre-main sequence (1289)

1. Introduction

The evolution of protoplanetary disks is thought to be closely interconnected to planet formation. As protoplanets grow in the disk, when they are massive enough, they dynamically open a gap around their orbital radius, a gap that can eventually separate the inner from the outer disk (e.g., M. F. Skrutskie et al. 1990; K. A. Marsh & M. J. Mahoney 1992; N. Calvet et al. 2002; P. D'Alessio et al. 2005). Disk winds are also expected to open gaps and eventually lead to disk dispersal, depleting disk gas that could otherwise be accreted by protoplanets (e.g., R. Alexander et al. 2014; B. Ercolano & I. Pascucci 2017; I. Pascucci et al. 2023). The relative distribution of dust and gas in inner disks could in principle inform which processes are driving disk evolution in different phases (e.g., C. Espaillat et al. 2014; C. F. Manara et al. 2023; N. van der Marel 2023).

Protoplanetary disks with an inner dust cavity have long attracted attention as a possibly particular phase during the global evolution from embedded objects (Class 0/I) to the final disk clearing stages (Class III and debris disks). This type

[19] These authors contributed proportionately to this work.
[20] NASA Hubble Fellowship Program Sagan Fellow.

of disk structure was first inferred from the analysis of spatially unresolved spectral energy distributions (SED) of pre-main-sequence stars showing a deficit in near-infrared (NIR) continuum emission in comparison to the median SED (often taken in Taurus) followed by a steeper rise toward the far-IR. These disks were interpreted as having an optically thin inner region and an optically thick outer region, implying significant depletion of small ($\lesssim\mu$m) dust grains from a hotter inner region suggestive of an "inside out" disk dispersal process. These disks became first known in the literature with the terms "transition/transitional (TD)" to highlight the evolutionary phase originally proposed as their interpretation (e.g., K. M. Strom et al. 1989; M. F. Skrutskie et al. 1990; D. W. Koerner et al. 1993; N. Calvet et al. 2002; P. D'Alessio et al. 2005; J. R. Najita et al. 2007; C. Espaillat et al. 2014; N. van der Marel et al. 2016).

With the availability of long-baseline interferometers, inner disk dust "cavities" or "holes" have later been spatially resolved in millimeter (mm) continuum emission, confirming and supporting, at first, the SED-based interpretation in a handful of disks (e.g., A. M. Hughes et al. 2007; J. M. Brown et al. 2009; S. M. Andrews et al. 2011), and providing new direct measurements of dust and gas clearings or depletion (e.g., J. P. Williams & L. A. Cieza 2011). After the advent of the Atacama Large Millimeter/submillimeter Array (ALMA), millimeter dust cavities have been spatially resolved in tens of disks, with a detection limit of $\gtrsim$5 au in cavity size with the long-baseline array but more often lower resolution, $\gtrsim$20 au, in large surveys of star-forming regions (e.g., M. Ansdell et al. 2016; I. Pascucci et al. 2016; P. Pinilla et al. 2018b; L. Francis & N. van der Marel 2020). With a larger number of spatially resolved disk cavities, the new interferometric surveys only partially matched earlier SED detections of inner dust evolution and called for new detection, classification, and analysis procedures (N. van der Marel 2023). Early SED-based classifications turned out to be in some cases affected by heterogeneous samples that mixed "TD" with "evolved" disks, which by showing a global SED decrease without a rise at far-IR wavelengths are now generally not considered anymore as having a dust cavity (C. Espaillat et al. 2014). Another typical source of uncertainty was the degeneracy in SED modeling due to dust properties, mass, disk geometry, and viewing angle (e.g., P. D'Alessio et al. 2006; E. Furlan et al. 2009; P. Woitke et al. 2016; N. P. Ballering & J. A. Eisner 2019; N. van der Marel et al. 2022).

On the other hand, several disks whose SED did not show any deficit in NIR continuum and therefore were not classified as "TD" have later been found to have a large millimeter cavity (R. A. Loomis et al. 2017; P. Pinilla et al. 2018a; N. van der Marel 2023). While the NIR continuum arises from small ($\lesssim\mu$m) dust, the millimeter emission is dominated by larger ($\gtrsim$mm) grains or particles, and these two different solid populations can naturally be spatially separated by their different aerodynamic coupling to the gas (Z. Zhu et al. 2011; A. Garufi et al. 2013; C. Espaillat et al. 2014). The wide range of cavity sizes, NIR continuum, and accretion rates indeed suggested early on that these disks might be an heterogeneous class of structures with different origins or observed in different conditions or phases of the same process (e.g., planets with different masses and/or coupled to winds of different nature or dead zones, see, e.g., reviews by J. R. Najita et al. 2007; C. Espaillat et al. 2014; B. Ercolano & I. Pascucci 2017; N. van der Marel 2023). In particular, planet-induced gaps can produce an inner disk clearing from millimeter dust grains by trapping them at larger radii while still allowing smaller dust to filtrate through the cavity, effectively producing a millimeter cavity that may or may not show an NIR deficit depending on the details of gas and dust coupling and evolution (e.g., W. K. M. Rice et al. 2006; Z. Zhu et al. 2012).

In terms of gas, disks with a dust cavity (identified from millimeter and/or SED studies) were found to have substantial stellar accretion rates indicating gas-rich inner regions (C. F. Manara et al. 2014), but with lower median accretion as compared to full disks in T Tauri stars with similar dust mass (J. R. Najita et al. 2007; and Section 2). Spatially resolved observations later demonstrated various degrees of gas depletion inside a dust cavity, generally supporting disk clearing by giant planets (e.g., A. Dutrey et al. 2008; N. van der Marel et al. 2015, 2018). Velocity-resolved infrared (IR) and UV line profiles have shown that at least CO and H_2 emit from a similar region well within the millimeter cavity (T. W. Rettig et al. 2004; K. M. Pontoppidan et al. 2008; C. Salyk et al. 2009; K. Hoadley et al. 2015; G. W. Doppmann et al. 2017; A. Banzatti et al. 2022), supporting modeling expectations for their density-dependent survival within the millimeter cavity (S. Bruderer 2013). While rovibrational CO emission is typically found to extend within the inner dust radius from IR interferometry, suggesting CO survival within a dust-free gas-dense region, disks with a dust cavity have typically shown narrower lines implying a recession of CO to larger radii (C. Salyk et al. 2009, 2011a; A. Banzatti & K. M. Pontoppidan 2015; A. Banzatti et al. 2017, 2022). The dependence of CO gas survival on residual dust within a millimeter cavity has indeed been confirmed in a large sample of disks around Herbig Ae/Be disks, by finding that CO emission recedes to larger radii with the decrease of NIR excess within the cavity (A. Banzatti et al. 2018).

Spatially and spectrally unresolved Spitzer spectra showed that disks with an NIR deficit have lower molecular luminosity or do not show molecular detections in H_2O, HCN, and C_2H_2 except for CO and OH (K. M. Pontoppidan et al. 2010; J. R. Najita et al. 2010; C. Salyk et al. 2011b). Follow-up analyses found at least one large millimeter cavity with an IR molecular spectrum very similar to a full disk (DoAr 44 with a millimeter cavity of ~40 au in C. Salyk et al. 2015, 2019), which was attributed to residual dust within the cavity previously inferred from SED modeling (C. Espaillat et al. 2010) and later spatially resolved at ~0.14 au with GRAVITY (J. Bouvier et al. 2020). A combined analysis of Spitzer and ground-based velocity-resolved spectra later showed that, as CO rovibrational lines get narrower in disks developing an inner dust cavity, the high-energy water emission decreases while the lower-energy emission is still strong at longer wavelengths, suggesting a joint sequential depletion from hotter to colder molecular gas. We illustrate this sequential depletion in Figure 1, which updates what is previously shown with Spitzer and ground-based data in Figure 9 in A. Banzatti et al. (2017). With JWST, the study of molecular gas in disk cavities is already expanding our knowledge, finding previously undetected water in PDS 70 (G. Perotti et al. 2023), a rich molecular spectrum in SY Cha (K. R. Schwarz et al. 2024), and rare species like CH_3^+ in TW Hya and GM Aur (T. Henning et al. 2024; C. E. Romero-Mirza et al. 2025).

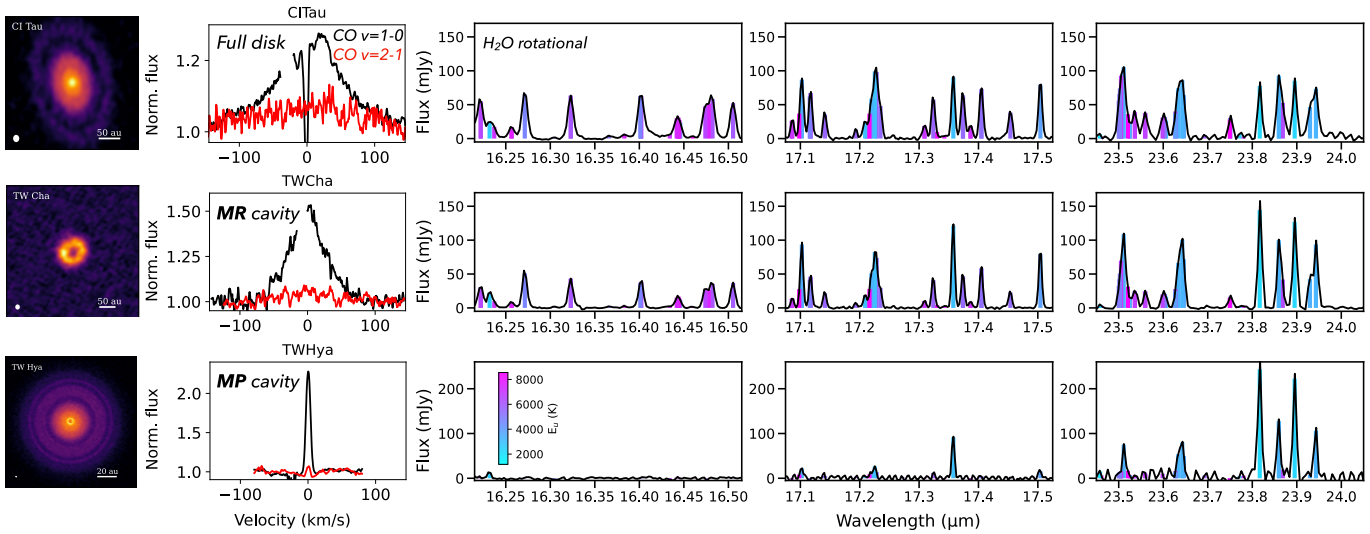

Figure 1. Inside out depletion of CO and water vapor previously observed with ground-based and Spitzer spectra in A. Banzatti et al. (2017), here reproduced with the new MIRI spectra, marking water transitions according to their upper level energy as in A. Banzatti et al. (2025). Three disks are shown as examples of a full disk and the molecule-rich (MR)/molecule-poor (MP) cavity types introduced in this work. As CO lines get narrower (plots on the left, with data from J. M. Brown et al. 2013; A. Banzatti et al. 2022), indicating depletion of the higher-velocity hot gas at $\lesssim$0.1 au, the higher-energy water lines (colored purple and magenta) become weaker while the lower-energy lines (blue and cyan) probing colder water at larger radii are still strong. ALMA continuum images are reported on the left for reference (see Section 2.2).

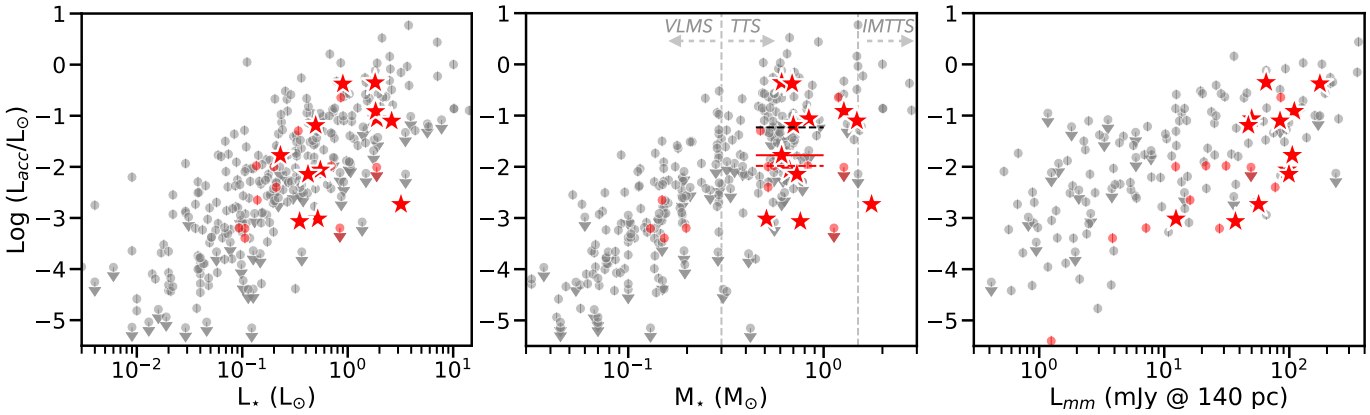

Figure 2. Comparison between the sample of cavity disks included in this work (red stars) and the large protoplanetary disk sample compiled in C. F. Manara et al. (2023) in gray and red dots. $L_{\rm acc}$ values for this work are estimated from MIRI spectra (Section 3.1). Disks labeled in C. F. Manara et al. (2023) as having a dust cavity are marked in red. The millimeter luminosity $L_{\rm mm}$, taken as the flux density normalized to 140 pc as in S. M. Andrews et al. (2018b), is taken at 1.3 mm, where the emission is more optically thin than at 0.89 mm and should better reflect the dust mass. The approximate boundaries between T Tauri stars (TTS), very-low-mass stars (VLMS), and intermediate-mass T Tauri stars (IMTTS) are marked for reference (N. Calvet et al. 2004; K. L. Luhman et al. 2010). The horizontal lines at stellar masses of 0.45–1 $M_{\odot}$ show the median log $L_{\rm acc}$ value for full disks (black), the cavity disks from C. F. Manara et al. (2023; dashed red), and the cavity disks in this work (solid red).

In this work, we assemble the first sample of disks with a dust cavity (see Section 2.1 for details on the selection) that have been observed with JWST-MIRI and expand on previous results to investigate molecular survival specifically in the disks of young pre-main-sequence stars of solar mass (T Tauri stars). We find that the high-quality MIRI spectra clearly show a dichotomy in molecular emission in these disks, which we use to formally define two types of inner disk cavities (Section 3): molecule rich (MR) and molecule poor (MP). Bearing in mind that the sample in this work is still small (12 objects) and thus requires further investigations with larger samples (see comparison to C. F. Manara et al. 2023; in Figure 2), we start in this work to identify the specific properties of MR and MP cavities and discuss them in the context of different levels of dust filtration through the millimeter cavity and of a gas density decrease, which we discuss in the context of a common evolution or different origins (Section 4).

In this work, we refrain from using the original interpretation-based term "TD," and we use instead the observation-based terms of "mm-cavity" disk if it has a spatially resolved millimeter dust cavity and "IR-cavity" disk if it has the IR index $n_{13-26} > 0$ that may indicate depletion of smaller dust in the inner disk (see Section 2 and Appendix B). We use "cavity disk" as a general term and "mm+IR cavity" disk to indicate that it has a cavity detected in both tracers. Protoplanetary disks without detected deficits in either tracer are identified as "full" disks and are used as a reference to analyze what is observed in disks with a dust cavity. These full disks may have gaps at multiple radii that are observationally different from a dust cavity in being (generally) radially narrower and having a large spatially resolved, optically thick inner disk in millimeter

Table 1
Sample Properties for Cavity Disks Studied in This Work

Name	Dist (pc)	$T_{\rm eff}$ (K)	$M_\star$ ($M_\odot$)	$L_\star$ ($L_\odot$)	log $L_{\rm acc}$ ($L_\odot$)	$R_{\rm disk}$ (au)	$L_{\rm mm}$ (mJy)	CO Width (km s^{-1})	$R_{\rm CO}$ (au)	n_{13-26}	$R_{\rm cav}$ (au)	Dust Cavity	Age (Myr)
Molecule rich (MR)													
SR 4	134	4115	0.61	1.82	−0.35	31	65.27	118–55	0.02–0.11	0.75	< 2.5	IR	$0.6^{+0.1}_{-0.1}$
HP Tau	177	4375	0.84	1.89	−1.06	22	50.04	117–41	0.02–0.18	0.36	< 10	IR	$0.8^{+0.5}_{-0.3}$
Sz 129	160	4020	0.73	0.42	−2.15	76	99.30	NA	NA	0.68	10	mm+IR	$3.8^{+3.3}_{-1.7}$
IP Tau	129	3792	0.51	0.52	−3.02	36	12.41	∼150–108[a]	0.04–0.08[a]	−0.06	25	mm(+IR)	$1.4^{+1.1}_{-0.6}$
TW Cha	183	4020	0.7	0.50	−1.19	53	47.05	132–63	0.05–0.23	0.19	30	mm+IR	$2.8^{+2.3}_{-1.3}$
SY Cha	181	4020	0.67	0.55	−2.06	184	96.16	∼250–200[a]	0.02–0.04[a]	−0.10	36	mm	$2.6^{+2.2}_{-1.2}$
Molecule poor (MP)													
TW Hya	60	3800	0.61	0.23	−1.78	58	105.61	12.9-7.3	0.2-0.6	1.19	2.4	mm+IR	$5.6^{+5.6}_{-2.7}$
HD 143006	167	4870	1.48	2.61	−1.10	81	84.29	28–22	1.68–2.55	1.55	6	mm+IR	$1.7^{+1.2}_{-0.7}$
T Cha	103	5300	1.76	3.2	−2.73	63	56.83	…[b]	…[b]	2.35	36	mm+IR	$2.9^{+2.2}_{-1.2}$
GM Aur	141	4115	0.69	0.91	−0.38	160	175.68	77–42[a]	0.26–0.89[a]	2.29	40	mm+IR	$1.3^{+0.8}_{-0.5}$
RY Lup	158	4710	1.27	1.84	−0.92	135	109.67	99–25	0.29–4.6	0.65	67	mm+IR	$1.9^{+1.4}_{-0.8}$
PDS 70	112	4138	0.76	0.35	<−3.07	110	37.12	NA	NA	−0.22	74	mm	$4.5^{+3.8}_{-2.0}$

Notes. Targets are separated into MR and MP following this work, and are ordered by mm-cavity size $R_{\rm cav}$ in each group. References: distances are from Gaia DR3 parallaxes (Gaia Collaboration et al. 2016, 2023), stellar properties are from C. F. Manara et al. (2023), which reports $T_{\rm eff}$ from G. J. Herczeg & L. A. Hillenbrand (2014), except for those not included in that work, TW Hya from M. Fang et al. (2018), PDS 70 from S. L. Skinner & M. Audard (2022), and T Cha from J. M. Alcala et al. (1997). $L_{\rm acc}$ is derived in this work from HI lines observed with MIRI using relations from B. M. Tofflemire et al. (2025). The infrared index n_{13-26} is measured from the MIRI spectra in this work (Appendix B). $R_{\rm disk}$ (the disk radius including 90%–95% of the millimeter emission depending on what is reported in different works) and disk inclinations are from J. Huang et al. (2018) and F. Long et al. (2019). The luminosity at 1.3 mm, $L_{\rm mm}$, is obtained by scaling the millimeter flux at 140 pc as done in S. M. Andrews et al. (2018b), with fluxes from M. Ansdell et al. (2016), D. Lommen et al. (2007), S. M. Andrews et al. (2018a), E. Macías et al. (2021), F. Long et al. (2019), R. Orihara et al. (2023), D. Fasano et al. (2025), and F. Long et al. (2025, in preparation). Ground-based near-infrared CO line widths observed with iSHELL and CRIRES (J. M. Brown et al. 2013; A. Banzatti et al. 2022) are measured at the 10% and 50% of the line peak from the stacked profiles (the values given in the table are the half line width velocities at 10% and 50%, or FW10%–FW50%); $R_{\rm CO}$ is the Keplerian radius from these velocities.

[a] In these disks, CRIRES and NIRSPEC observe a stellar photospheric spectrum with weak and broad emission in SY Cha and narrow emission in GM Aur (see spexodisks.com, C. H. Wheeler et al. 2024); the line widths in GM Aur are adopted from C. Salyk et al. (2009), and in IP Tau are from G. W. Doppmann et al. (2017). $R_{\rm cav}$ is the cavity radius as determined from spatially resolved ALMA images taken at the peak of the first dust ring limiting the cavity, as reported in J. Huang et al. (2018, 2020), L. Francis & N. van der Marel (2020), N. van der Marel (2023), and references therein, except for TW Hya from S. M. Andrews et al. (2016) and TW Cha from F. Long 2025 (private communication). The stellar age was determined using the tool from D. Deng et al. (2025) based on the IDL code developed by I. Pascucci et al. (2016), which uses evolutionary tracks of G. A. Feiden (2016) for sources with $T_{\rm eff} > 3900$ K and that of I. Baraffe et al. (2015) for $T_{\rm eff} \leqslant 3900$ K.

[b] In the case of T Cha, CO lines detected in CRIRES spectra include both emission and absorption and do not provide an estimate of the emission line profile (J. M. Brown et al. 2013).

emission. These disk structures might still be sequential in terms of evolution, as it has been proposed that planet-induced gaps may later develop into cavities in the context of the formation of giant planets through core accretion (S. E. Dodson-Robinson & C. Salyk 2011; L. A. Cieza et al. 2021; S. Orcajo et al. 2025).

2. Sample and Observations

2.1. Sample Definition and Properties

The selection of 12 disks for this work is based on Class II protoplanetary disks that have an identified dust cavity and are available from a number of Cycle 1 and 2 JWST-MIRI programs (see Section 2.2). Sample properties, including the cavity type in each disk, are reported in Table 1 and are visualized in Figure 2 to put the sample into a broader context, illustrating that it is composed of stars with a mass of 0.5–1.5 $M_\odot$ with relatively millimeter-bright disks. The cavity identification is based on ALMA images complemented with the slope at IR wavelengths as measured directly from the JWST-MIRI continuum, both of which have their own limitations in revealing a disk cavity (see Section 1 and Appendix B). The selection of millimeter-cavity disks is based on high-resolution ALMA images, which directly resolve cavities in millimeter dust continuum emission; the limitation of this selection is that ALMA images can still miss small cavities with a size <5–20 au depending on the spatial resolution achieved in nearby star-forming regions at 120–200 pc in different works (Section 1). In this work, 10 of 12 disks have a spatially resolved disk cavity in millimeter emission (Table 1).

The second type of data we use is the JWST-measured IR index n_{13-26} (formerly the n_{13-30} index when measured from Spitzer spectra) that measures the slope of the SED between 13 and 26 μm and is sensitive to the depletion of small ($\lesssim\mu$m) dust in the inner hot disk region (J. M. Brown et al. 2007; E. Furlan et al. 2009). While different limits have been adopted in the past to identify a dust cavity based on the IR index, based on spatially resolved cavities and SED modeling, A. Banzatti et al. (2020) discussed that an inner dust cavity may be revealed by $n_{13-30} \gtrsim 0$, now $n_{13-26} \gtrsim 0$ with MIRI (see Appendix B). In this work, 9 of 12 disks have an IR cavity based on their positive n_{13-26} index (plus two border-line cases with negative index of ~ -0.1), of which 7 of 12 have

both a millimeter and an IR deficit (mm+IR cavity, Table 1). It should be considered that the IR SED (and therefore the IR index) is known to be variable in disks that have a cavity (C. Espaillat et al. 2011; C. C. Espaillat et al. 2024; C. Xie et al. 2025), which will produce scatter in indices measured at different times (see Appendix B). An important example to mention is the case of PDS 70 (discussed in Appendix D), which in this work shows only a millimeter cavity by having a negative IR index, but using a previous Spitzer spectrum, it would have a positive index and be a mm+IR cavity (G. Perotti et al. 2023; H. Jang et al. 2024).

Disk models show that the SED at 10–30 μm is sensitive to the removal of $\lesssim\mu$m dust in a region as small as $\sim$1–2 au (e.g., P. Woitke et al. 2016; N. P. Ballering & J. A. Eisner 2019) and therefore can reveal small cavities that ALMA may not be able to resolve. We include in this sample two disks that might be in this situation: SR 4 and HP Tau, which have significantly positive $n_{13-26} = 0.36$–0.75 but no cavity detected with ALMA at the current spatial resolution, providing an upper limit of $\lesssim$2.5 au and $\lesssim$10 au for a dust cavity, respectively (taking the upper limit to be given by FWHM/2 of the synthesized beam obtained in each case, J. Huang et al. 2018; F. Long et al. 2019). For comparison, TW Hya has a 2.4 au cavity, which is spatially resolved due to its much closer distance of only 60 pc (S. M. Andrews et al. 2016), and has an index $n_{13-26} \sim 1.2$ ($\sim$2–3 times larger than in HP Tau and SR 4). In case they do not have a dust cavity, HP Tau and SR 4 must have another explanation for their positive IR index that mimics a cavity. A high disk inclination can mimic a cavity (e.g., N. P. Ballering & J. A. Eisner 2019; N. van der Marel et al. 2022), but this possibility can be excluded in this case since these disks are almost face-on (S. M. Andrews et al. 2018a; F. Long et al. 2019). An alternative explanation proposed early on for positive IR indices in the range $\sim$0–0.5 is a dust/gas mass ratio closer to standard interstellar matter (ISM) values in the disk surface (dust/gas = 0.01–0.0001), while most Class II disks should be dust depleted by settling (dust/gas = 0.0001–0.00001, P. D'Alessio et al. 2006; E. Furlan et al. 2006, 2009). If these two disks are less settled or have dust/gas closer to ISM values, it may provide a reason for their positive index. In conclusion, in this work, we still include HP Tau and SR 4 in the sample of cavity disks by assuming they do have an unresolved dust cavity, and we adopt an upper limit on their cavity size as written above.

2.2. Observations

All disks were observed over the full wavelength coverage of 4.9–28 μm with the Medium Resolution Spectrometer (MRS; M. Wells et al. 2015) mode on MIRI (G. H. Rieke et al. 2015; G. S. Wright et al. 2023). The data come from the following programs, mostly from the JDISCS (K. M. Pontoppidan et al. 2024; N. Arulanantham et al. 2025) and MINDS (I. Kamp et al. 2023; T. Henning et al. 2024) collaborations: 3 disks from GO-1584 (PI: C. Salyk; co-PI: K. Pontoppidan), 3 disks from GO-1282 (PI: T. Henning; co-PI: I. Kamp), 2 disks from GO-1640 (PI: A. Banzatti), 1 disk from GO-1549 (PI: K. Pontoppidan), 1 disk from GO-2025 (PI: K. Öberg), 1 disk from GO-2260 (PI: I. Pascucci), 1 disk from GO-3228 (PI: I. Cleeves), for a total of 12 disks. All these MIRI spectra were previously published first in the following papers: G. Perotti et al. (2023), A. Banzatti et al. (2023), K. R. Schwarz et al. (2024), K. M. Pontoppidan et al. (2024), C. E. Romero-Mirza et al. (2024), T. Henning et al. (2024), N. S. Bajaj et al. (2024), A. D. Sellek et al. (2024), A. Banzatti et al. (2025), N. Arulanantham et al. (2025), and C. E. Romero-Mirza et al. (2025), except for IP Tau from C. E. Romero-Mirza et al. (2025, in preparation).

All MIRI-MRS spectra were extracted and wavelength calibrated with the JDISCS pipeline as described in K. M. Pontoppidan et al. (2024), which adopts the standard MRS pipeline (H. Bushouse et al. 2024) up to stage 2b producing the three-dimensional cubes and then uses observed asteroid spectra from GO program 1549 as calibrators to provide high-quality fringe removal and characterization of the spectral response function to maximize signal-to-noise ratio (S/N) in channels 2–4. A standard star is used in channel 1 where asteroid spectra have low S/N. To ensure similar fringes and maximize the quality of their removal, target acquisition with the MIRI imager was adopted to reach subspaxel precision in placing a science target and asteroids on the same spot on the detector. For the data included in this work, we used MRS pipeline version 12.1.5 with Calibration Reference Data System context jwst_1364.pmap and JDISCS reduction version 9.0 that includes an improved bad pixel correction and flux calibration uncertainty down to 1%–2% across MIRI. Before the analysis of molecular lines, the MIRI spectra were continuum subtracted with the procedure presented in K. M. Pontoppidan et al. (2024) updated to apply a wavelength-dependent offset correction based on line-free regions to account for gas absorption where present, as described in A. Banzatti et al. (2025). The MIRI spectra are illustrated in Appendix A.

In addition to MIRI spectra, we include dust measurements of inner dust cavities as measured in the millimeter continuum with ALMA (see references in Table 1). To illustrate the dust emission radial structures, we include some ALMA continuum images with data from S. M. Andrews et al. (2016, 2018a), F. Long et al. (2019), J. Huang et al. (2020), M. Benisty et al. (2021), and F. Long et al. (2025, in preparation), e.g., in Figure 1. To complement the limited kinematic information provided by MIRI spectra, we also include velocity-resolved *M*-band rovibrational CO emission observed with ground-based IR spectrographs (iSHELL and CRIRES, H.-U. Kaeufl et al. 2004; J. Rayner et al. 2022) from J. M. Brown et al. (2013) and A. Banzatti et al. (2022). Details on the data reduction and analysis of these datasets can be found in the original papers.

3. Analysis and Results

3.1. Defining Molecule-rich and Molecule-poor Cavities

Building on previous work that found a few exceptions to a general trend of low molecular detections in disks with dust cavities (see Section 1), in this work we use the higher-resolution MIRI spectra and new accretion estimates from MIRI to clearly define a classification of disk cavities based on their molecular spectra. As a reference for the observed gas properties in inner disks, we use the T Tauri disk sample from the JDISC Survey obtained in Cycle 1 (K. M. Pontoppidan et al. 2024; N. Arulanantham et al. 2025), after removing disks with cavities that are studied in this work (TW Cha, RY Lup, Sz 129, SR 4, HP Tau). We label this sample as "JDISCS-C1" in this work. This reference sample of full disks defines tight global trends and correlations with the accretion luminosity

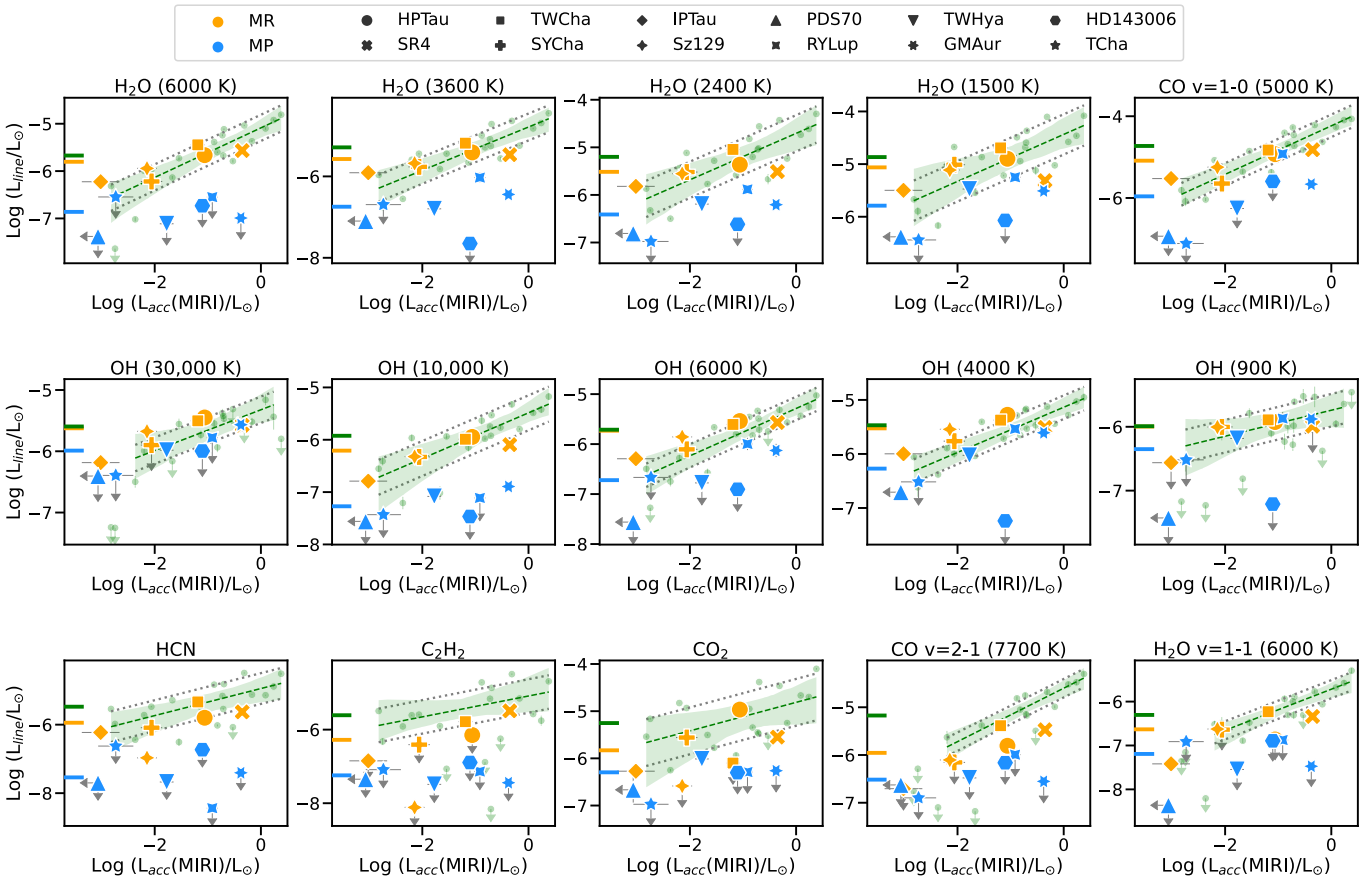

Figure 3. Line luminosity of multiple molecules as a function of accretion luminosity as measured in MIRI spectra. Where included, the number in Kelvin indicates the approximate upper level energy (see Table 3). The sample of disks with cavities is separated into "molecule rich" (MR, orange) and "molecule poor" (MP, blue) as defined in this work (see Section 3.1). The reference sample shown in green is composed of full disks in the JDISCS-C1 sample (Section 3.1), with linear fits and their 95% confidence intervals shown as dashed lines and shaded regions and regression parameters included in Appendix C. The dotted lines show one standard deviation of the distribution of full disks around each correlation, which is used to define MR cavities in the higher-energy water lines (Section 3). Median luminosity values for full, MR, and MP disks are shown as bars to the left in each panel. Higher-vibrational lines of CO and H_2O are included in the bottom row of plots for reference to the subluminous organics (see discussion in Section 4.3).

(Figure 3), which previous work found to be the strongest parameter driving the observed molecular line luminosities in T Tauri stars (A. Banzatti et al. 2020, 2025).

In Figure 3, we present the sample of cavity disks as compared to the correlations defined by full disks with the accretion luminosity $L_{\rm acc}$, which we measure from MIRI spectra using the three H I lines (10–7, 7–6, 8–7) following B. M. Tofflemire et al. (2025). The value we adopt is the weighted average of $L_{\rm acc}$ from these three lines where detected, and we show it as $L_{\rm acc}$(MIRI) in the figures in this work. While Balmer-jump fits typically provide the most reliable $L_{\rm acc}$ estimates, here, we use $L_{\rm acc}$ estimates from MIRI HI lines because they provide an accretion tracer simultaneous to the MIRI gas lines and because they give us $L_{\rm acc}$ for the entire sample used in this work. For reference, we note that if we use literature values for $L_{\rm acc}$, available from C. F. Manara et al. (2023) only for part of the sample and complemented with other papers where necessary, the trends and cavity disk dichotomy reported in Figure 3 do not change despite a slightly larger scatter that we attribute to time variability of $L_{\rm acc}$ (see also discussion of this topic in, e.g., R. A. B. Claes et al. 2022; S. A. Smith et al. 2025). In this analysis, we prefer to use the simultaneous H I-derived $L_{\rm acc}$ even if they may have more uncertain luminosity relations (E. Fiorellino et al. 2025; B. M. Tofflemire et al. 2025; B. Shridharan et al. 2025), or be potentially affected in some disks by jet contamination (N. S. Bajaj et al. 2024).

First, we report here the results for the reference JDISCS-C1 sample (green points and linear regressions in Figure 3) of full disks for a number of molecular lines. We adopt the line list defined in A. Banzatti et al. (2025) for H_2O and CO, and we add specific lines and ranges to measure OH across energy levels (similarly to what was done for the water lines) and organic emission as explained in Appendix C. The line luminosity of all of these molecules correlates significantly with $\log L_{\rm acc}$ and less with $\log L_\star$ (see regression results in Table 3), confirming previous results from Spitzer (A. Banzatti et al. 2017, 2020), and shows stronger correlation and steeper slopes for higher upper level energy, as recently found for H_2O lines from MIRI spectra (A. Banzatti et al. 2023, 2025). The organics show larger scatter but similar trends, with stronger correlation (excluding upper limits) and steeper slope for HCN and C_2H_2 in comparison to CO_2,[21] in line with their relative excitation temperatures that are found to be generally lower for CO_2, suggesting that it traces cooler gas (N. Arulanantham et al. 2025). Thermochemical models explain these correlations as a dependence of H_2O and OH emission on UV

[21] In the case of CO_2, part of the scatter could be due to residual contamination; see Appendix C.

Table 2
Detection Summary for Molecular Tracers in Cavity Disks Analyzed in This Work

Name	H_2O					OH					HCN	C_2H_2	CO_2	CO	CO
	6000	3600	2400	1500	$v = 1$–1	30,000	10,000	6000	4000	900				$v = 1$–0	$v = 2$–1
Molecule rich (MR)															
SR 4	√	√	√	√	√	√	√	√	√	⋯	√	√	√	√	√
HP Tau	√	√	√	√	⋯	√	√	√	√	√	√	⋯	√	√	√
Sz 129	√	√	√	√	√	√	√	√	√	√	√	⋯	⋯	√	√
IP Tau	√	√	√	√	√	√	√	√	√	⋯	√	⋯	√	√	⋯
TW Cha	√	√	√	√	√	√	√	√	√	√	√	√	⋯	√	√
SY Cha	√	√	√	√	⋯	⋯	√	√	√	√	√	⋯	√	√	⋯
Molecule poor (MP)															
TW Hya	⋯	√	√	√	⋯	√	√	⋯	√	√	⋯	⋯	√	(√)	⋯
HD 143006	⋯	⋯	⋯	⋯	⋯	⋯	⋯	⋯	⋯	⋯	⋯	⋯	⋯	(√)	⋯
T Cha	⋯	⋯	⋯	⋯	⋯	⋯	⋯	⋯	⋯	⋯	⋯	⋯	⋯	(√)	⋯
GM Aur	⋯	√	√	√	⋯	√	√	√	√	√	⋯	⋯	⋯	√	⋯
RY Lup	⋯	√	√	√	⋯	⋯	⋯	√	√	√	⋯	⋯	⋯	√	⋯
PDS 70	⋯	√	√	√	⋯	⋯	⋯	⋯	√	⋯	(√)	(√)	√	⋯	⋯

Note. Targets are ordered from smaller to larger millimeter-cavity size as in Table 1. Lines are considered detected if the measured line flux is greater than 2σ. See Appendix C for line definitions, spectral ranges, and line flux and error measurements. In the case of H_2O and OH lines, the column header identifies each line as done in Figure 3. CO is detected in TW Hya, HD 143006, and T Cha with ground-based spectrographs, but not with MIRI. See Appendix D for tentative detections in PDS 70.

luminosity, which dominates L_{acc}, while organic emission should mostly depend on X-ray luminosity instead (P. Woitke et al. 2024; see also Section 4.3), consistent with the lower correlation and larger scatter in their trends with L_{acc}.

Once these global trends are defined by the reference sample of full disks, a comparison to disks with cavities in Figure 3 demonstrates the dichotomy that is the main focus of this work. We base the classification on the H_2O higher-energy lines (3600–6000 K, top row of plots in the figure), which are some of the most reliable, high S/N lines and probe the inner hotter molecular gas on a region that has been found in previous work to reflect the formation of an inner disk cavity (A. Banzatti et al. 2017; C. Salyk et al. 2019; and Figure 1). Specifically, we measure the deviation of cavity disks from the best-fit correlation and compare it to the standard deviation of the distribution of full disks around the best-fit line. Half of the disk cavity sample in this work is consistent with full disks within one standard deviation in both the 3600 and 6000 K H_2O lines, making them indistinguishable from a full disk; we call these "MR" cavities (see, e.g., the example of TW Cha in Figure 1) and mark them in orange in all figures.

The other half of the sample is consistently subluminous in most other molecular lines, especially in the hot ($T > 400$ K) molecular gas tracers. We call these "MP" cavities (see, e.g., example of TW Hya in Figure 1) and mark them as light blue data points in all figures. In other words, the distinction we define here with MR and MP is between a disk cavity that has molecular emission as luminous as a full disk that has similar stellar and accretion luminosity, or rather, it is significantly subluminous (see Table 2 for a detection summary) indicating molecular depletion as we will discuss in Section 4. This dichotomy is visible but reduced in the colder gas tracers, especially the lower-energy H_2O and OH lines. This difference in the depletion of higher versus lower-energy water lines confirms what was previously observed from the combination of Spitzer and CRIRES data, where water emission in cavity disks was observed to reduce from higher- to lower-energy levels suggesting depletion from hotter to colder molecular gas in an inside out fashion (Figure 9 in A. Banzatti et al. 2017; and Figure 1 in this work).

It is worth noting some important exceptions. Organic emission is on-average subluminous in all cavities including the MR, although not as extreme as in the MP cavities (Figure 3). This is especially visible in C_2H_2, which is firmly detected only in two MR cavities. A drop in line luminosity is also observed in the CO $v = 2$–1 and, to a lesser extent, the H_2O $v = 1$–1 lines, which tend to be on-average subluminous in all disk cavities, including MR. This will be discussed in Section 4.3. The OH lines, instead, show distinct behavior as a function of upper level energy across the MIRI spectrum. The highest-energy lines populated by prompt emission following water photodissociation ($E_u > 20{,}000$ K emitting at <11 μm) are slightly superluminous in MR cavities, and consistent with full disks in MP (but only detected in GM Aur and TW Hya). OH lines with E_u of 6000–10,000 K are consistent with full disks in MR cavities, and subluminous in MP cavities. Going to lower energies, OH lines with $E_u = 4000$ K are again slightly superluminous in MR and slightly subluminous in MP cavities as compared to full disks. The lowest-energy OH lines covered with MIRI, the $E_u \sim 900$ K lines at 24.64 μm, show that MR cavities have luminosity generally consistent with the full disks.

Figure 4 follows Figure 3 but shows molecular luminosities as a function of the IR index n_{13-26} as measured in MIRI spectra (Appendix B). The trends between molecular luminosity and n_{13-26} generally confirm results from Spitzer previously reported in C. Salyk et al. (2011b) and A. Banzatti et al. (2020): molecular luminosities have an anticorrelation with n_{13-26} that is consistent with a linked depletion of inner disk small dust grains and molecular gas. In this work, we improve previous Spitzer results in two ways. First, full disks on their own show in many cases (especially in higher-energy lines, see results in Table 3) anticorrelations between the line luminosity and n_{13-26} even extending to negative values of the

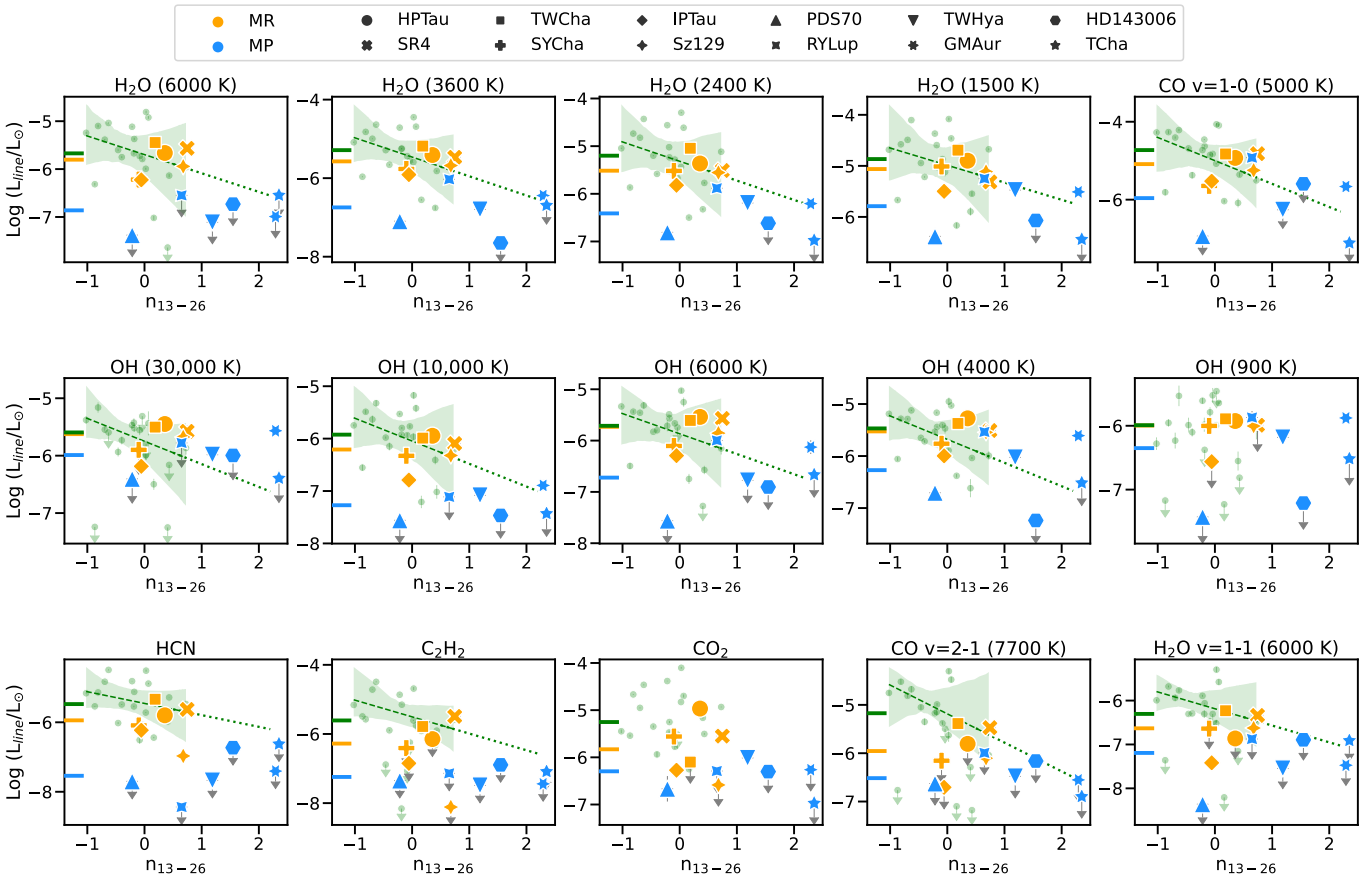

Figure 4. Same as Figure 3 but showing the infrared index n_{13-26}, the slope in the SED between 13 and 26 μm. Linear fits to the full disks and their 95% confidence intervals are shown as dashed lines and shaded regions when considered detected (absolute value of the Pearson coefficient >0.25), with regression parameters included in Table 3. Dotted lines show extrapolations of full-disk linear fits when a correlation is detected in the full disks, for comparison to the distribution of cavity disks.

index (which may correspond to different levels of dust settling in full disks, see Appendix B and Section 4). Exceptions are the 900 K OH lines and CO_2, where a correlation is not detected in the full disks alone. Second, MR cavities generally overlap with one end of this correlation (at $n_{13-26} \sim 0$) while the MP cavities are generally consistent with decreasing trends with n_{13-26}. The disk of PDS 70 appears as an outlier in all of these plots for its low n_{13-26}; the inner dust disk in this system is known to be variable (G. Perotti et al. 2023; E. Gaidos et al. 2024; H. Jang et al. 2024; and Appendix B), and it will be discussed in Section D.3.

3.2. Water Spectra in Disk Cavities

Focusing now on the excitation of water spectra, disks with cavities show properties that reflect the decrease in the high-energy lines, a decrease in column density, and the dominance of colder water. These properties are illustrated in Figure 5 with the diagnostic diagrams introduced in A. Banzatti et al. (2025), where line ratios at different E_u are sensitive to the relative emitting area and column density of water reservoirs across a temperature gradient from the inner dust rim out to the snowline (for a simple interpretation of each diagnostic, see labels in Figure 5). The MR/MP dichotomy of inner disk cavities defined in the previous section and Figure 3 reveals how they evolve in comparison to full disks in these diagrams. MR cavities have the 6000 K H_2O line luminosity (which can be interpreted as mostly driven by the size of the emitting region) comparable with those measured in full disks with relatively small areas, while MP cavities are systematically lower than most of the full disks (left plot in Figure 5). The luminosity of the 1500 K H_2O lines is instead more similar in MR and MP cavities, as already shown in Figure 3. Cavity disks in general show a higher 3340 K line ratio, where detected, that is consistent with a factor of $\gtrsim$10 lower column density of the warm water component in comparison to the majority of full disks (middle plot). The only exception among the cavity disks is PDS 70, which has the lowest value of the 3340 K line ratio consistent with the higher column density measured in most full disks; this will be discussed in Section D.3.

Overall, the sample of cavity disks sits at the higher right in the 3600/6000 K and 1500/3600 K diagram in comparison to the full disks, indicative of water spectra being increasingly dominated by colder emission in cavity disks (right plot in Figure 5). The MR cavities are consistent with a similar temperature gradient as in full disks (assuming $T = T_0(r/0.5\text{au})^{-\alpha}$ as in C. E. Romero-Mirza et al. 2024; A. Banzatti et al. 2025) and have higher 1500/3600 K ratios indicative of relatively larger cold water areas (right plot, compare to full disks in Figure 22 in A. Banzatti et al. 2025). MP cavities sit at the extreme right of the plot due to their much lower hot water luminosity, indicating even shallower temperature gradients that may in some cases be well reproduced by a single warm (~400 K) component (similar

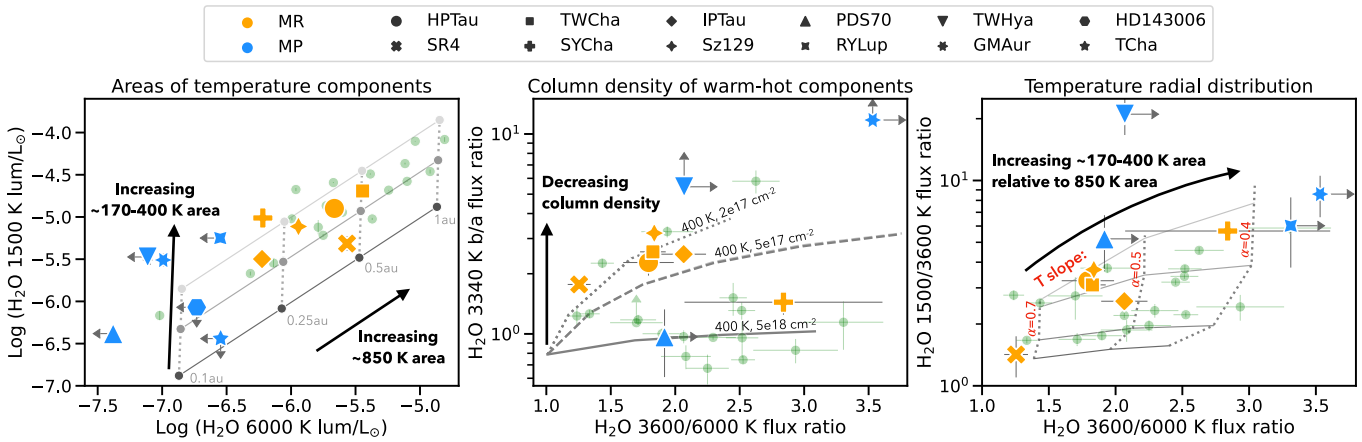

Figure 5. Water diagnostic diagrams defined in A. Banzatti et al. (2025), with arrows to indicate the main directions for simple empirical interpretations based on multicomponent slab models in LTE. As in Figure 3, MR cavities have 6000 K H_2O luminosities comparable with those measured in full disks, while MP cavities are significantly subluminous (left plot). Cavity disks in general show a lower column density of the warm-hot water components (middle plot). The diagnostic line ratios in MR cavities show a similar temperature slope as in full disks but show a relatively stronger colder water reservoir (right plot). MP cavities tend to cluster at the top right of the plot due to their decreased hot water luminosity.

to the case of MY Lup in C. Salyk et al. 2025). The 3600/6000 K and 1500/3600 K ratio values measured in MP cavities are consistent with two disks identified in M. Temmink et al. (2025) as being "water poor" (DN Tau and CX Tau). The authors proposed those disks could have a small inner cavity; CX Tau, with $n_{13-26} \sim 0$ as measured in MIRI, is indeed a good candidate for an unseen small inner dust cavity, while DN Tau, with $n_{13-26} \sim -0.16$, is less so, especially without evidence for a millimeter cavity at high angular resolution (F. Long et al. 2019).

In terms of the coldest water detected with MIRI, the diagnostic line ratios in Figure 6 show that cavity disks have values overlapping to those in full disks (similar to what is found in the diagram in Figure 5), but overall, they tend to have higher 1500/6000 K ratios as well as higher 1448/1615 K ratios, consistent with 170–200 K water in all disks. This diagram suggests that, as the hot water reservoir is decreased in a disk cavity, the spectrum is dominated by colder water near the snowline (see more in Section 4).

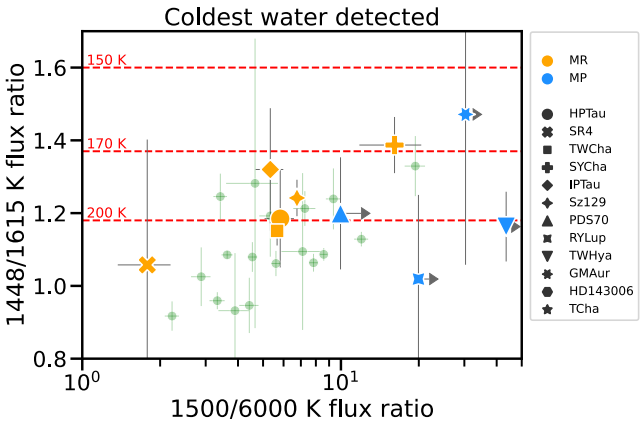

Figure 6. Cold water diagnostic diagram defined in A. Banzatti et al. (2025) based on the line flux ratio between the two low-energy lines near 23.85 μm. Excitation temperatures labeled in red assume LTE and a column density of 10^{17} cm^{-2}. Cavity disks tend to have larger line ratios on both axes as indicative of colder water emission than in full disks, with MP cavities clustering at the right of the plot due to the decreased hot water luminosity as in Figure 5.

3.3. OH Emission and H_2O Photodissociation

Figures 3 and 4 show that OH emission in all cavity disks tends to be as luminous or slightly superluminous in comparison to trends defined by full disks as a function of L_{acc} or n_{13-26}, in contrast to other molecules that show a luminosity decrease at least in MP cavities (if not even in MR cavities, as the case of organics). Due to its efficient reformation, OH is one of the most persistent molecules that is often a tracer of UV irradiated environments and of water photodissociation (e.g., A. Tappe et al. 2008; D. Fedele et al. 2013; A. Parikka et al. 2017). Thanks to the large range of energy levels covered by MIRI spectra, it is now possible to investigate different gas reservoirs because OH is expected to trace a similarly extended radial gradient to water in inner disks (a surface layer higher up in the disk atmosphere, e.g., P. Woitke et al. 2018, 2024) as well as the highly excited OH lines from photodissociation of water (A. Tappe et al. 2008; J. S. Carr & J. R. Najita 2014; B. Tabone et al. 2021). Specifically, levels of >20,000 K should unambiguously be populated by photodissociation of water showing the characteristic flux asymmetry in OH doublets (e.g., D. A. Neufeld et al. 2024), sometimes detected down to levels of ~10,000 K (in the MP disk of GM Aur, C. E. Romero-Mirza et al. 2025), while lower-energy levels emitting from longer wavelengths could be increasingly populated by chemical pumping (B. Tabone et al. 2024; M. Zannese et al. 2024).

The 30,000 K lines are equal to or superluminous in cavity disks in comparison to the trend defined by full disks. The flux of these lines is proportional to the amount of H_2O photodissociated per unit of time, not to the OH abundance, and may simply trace a UV irradiated surface layer where OH is abundant and H_2O is underabundant, where H_2O is constantly photodissociated back to OH (B. Tabone et al. 2021; M. Zannese et al. 2024). The ratio of these very high-energy lines to the 6000 and 4000 K lines, which are likely excited by chemical pumping, is higher in MP disks and shows some correlation with n_{13-26} (Figure 7). Significant trends are also observed in the OH/H_2O line ratios with similar upper level energy, which might trace a radial gradient of these two molecules from a hotter inner region to a colder region at larger radii. The OH/H_2O ratios are on average higher in

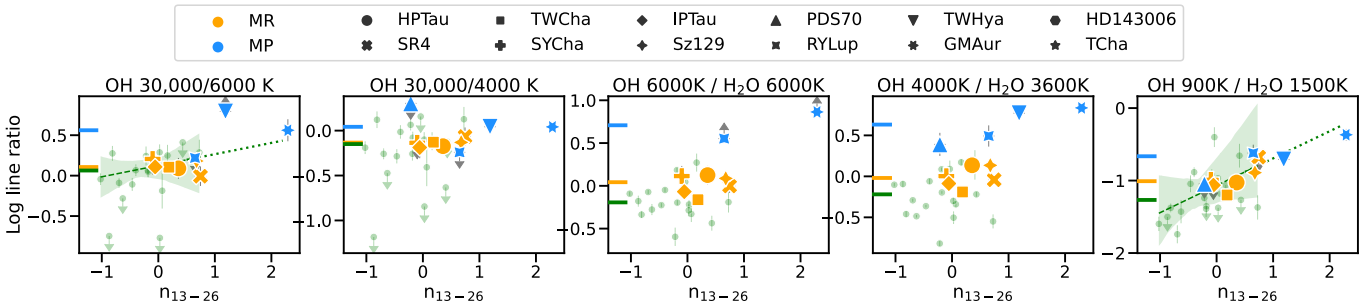

Figure 7. Same as Figure 4 but showing line flux ratios between OH lines or OH and H_2O lines over a range of upper level energy. Higher median OH/H_2O ratios are observed in all cavity disks (including MR) in comparison to full disks across energy levels, consistent with a higher H_2O photodissociation.

cavity disks in comparison to full disks across all energy levels included in MIRI (Figure 7), possibly indicating increased water photodissociation as the inner disk is becoming depleted from the shielding dust. A significant correlation is detected in the ∼4000 K OH/H_2O line ratio in the MP disks, and the colder OH lines covered by MIRI (∼900 K at 24.6 μm, the most likely tracer of a collisionally populated reservoir) show a correlation with n_{13-26} in all disks (Figure 7). These trends may be due to the different response to UV irradiation and dust removal, causing the dissociation and recession of water to larger radii while OH persists. Given the complexity of non-LTE OH excitation, all these trends should be investigated in future thermochemical modeling work to clarify their origin.

4. Discussion

With the improved line luminosity measurements from MIRI spectra (in sensitivity and deblending, compared to Spitzer) and simultaneous accretion luminosity estimated from mid-IR H I lines, the new MIRI-MRS spectra expand on previous Spitzer and ground-based results and demonstrate a dichotomy in molecular emission observed from disks that have a millimeter dust cavity (Section 3). Disk cavities are either very similar to full disks from the point of view of their IR molecular emission (named MR in this work), although they still tend to show subluminous emission from organics and in particular from C_2H_2, or are subluminous in all the molecular emission except for OH lines in some cases (named MP). In this section, we describe the properties emerging from the sample included in this work for the two types of disk cavities and discuss their potential interpretations in terms of inner disk evolution.

4.1. Sample Properties of MR versus MP Disk Cavities

In Figure 8, we present the emerging properties for the dichotomy into MR and MP cavities as defined in this work. The sample includes cavities as small as ∼2 au and as large as 70 au, with IR index between −0.2 (indicating residual inner hot dust within the millimeter cavity) and up to ∼2.4 (indicating significant dust depletion within the millimeter cavity). MR cavities have IR index in the range $-0.2 \lesssim n_{13-26} \lesssim 0.75$ with a trend of decreasing n_{13-26} for increasing millimeter-cavity sizes at least up to 40 au (bottom left panel in Figure 8). MP cavities, on the contrary, have $n_{13-26} \gtrsim 1$ with increasing value for cavities up to ∼40 au, and then decreasing n_{13-26} value up to ∼70 au. The discovery of this bifurcation into these two global trends is remarkable, since the index n_{13-26} should reflect more the radial distribution of (sub)μm dust rather than the truncation of millimeter grains outside a cavity (see also Appendix B). This bifurcation is one of the fundamental findings of this work supporting a dichotomy in molecular emission, as we will discuss below (we will also show in Section 4.6 that the bifurcation of MR and MP in this parameter space is supported by increasing the sample).

In this sample of T Tauri stars (we do not include any $T_{\rm eff} > 5500$ K in this work), MP cavities equally split between subsolar and supersolar stellar masses, while MR cavities only have subsolar masses (Figure 8). This supports previous findings that stars earlier than K5 more frequently have millimeter+IR cavity while stars later than K5 more frequently have a millimeter cavity that does not show an NIR deficit (N. van der Marel 2023). The two cavity types, however, are not separated in accretion luminosity and show an $L_{\rm acc}$ range similar to that of full disks, although with a lower mean, supporting in this regard previous findings about lower accretion in disk cavities in general (Section 1). The millimeter luminosity is comparable in both MR and MP and the full disk sample with no clear trend with n_{13-26}, suggesting that the observed mass in millimeter grains may be similar or slightly larger in MP cavities (for the caveats of converting single-frequency millimeter continuum flux into an estimate of disk solid mass see, e.g., A. Miotello et al. 2023). The age spread of MR and MP is also similar, but MP include older objects, and the mean age difference between MP and MR is ∼1 Myr in this sample (lower for MR); a potential decrease in molecular emission with time has recently been proposed in C. E. Romero-Mirza et al. (2025), where GM Aur and other disks classified as MP in this work were proposed to be older than SY Cha,[22] classified MR in this work. The cavity disks in this sample are instead, on average, definitely older than the JDISCS-C1 full disk sample, where ages are obtained in the same way and adopted from K. Zhang et al. (2025, in preparation).

In reference to previous findings from rovibrational CO lines as velocity resolved from the ground, which showed a recession of CO and H_2O to larger radii in disk cavities (A. Banzatti et al. 2017; and Figure 1), we now find that the CO inner emitting radius shows a clear separation between MR cavities, which have broad CO emission extending well into 0.01–0.1 au (fully consistent with where CO is observed in full disks), and MP cavities, where instead high-velocity CO

[22] While C. E. Romero-Mirza et al. (2025) adopted ages from different literature works, by using the tool by D. Deng et al. (2025), in this work, we actually find a younger age for GM Aur and older for SY Cha; individual stellar ages are known to be uncertain (D. R. Soderblom et al. 2014).

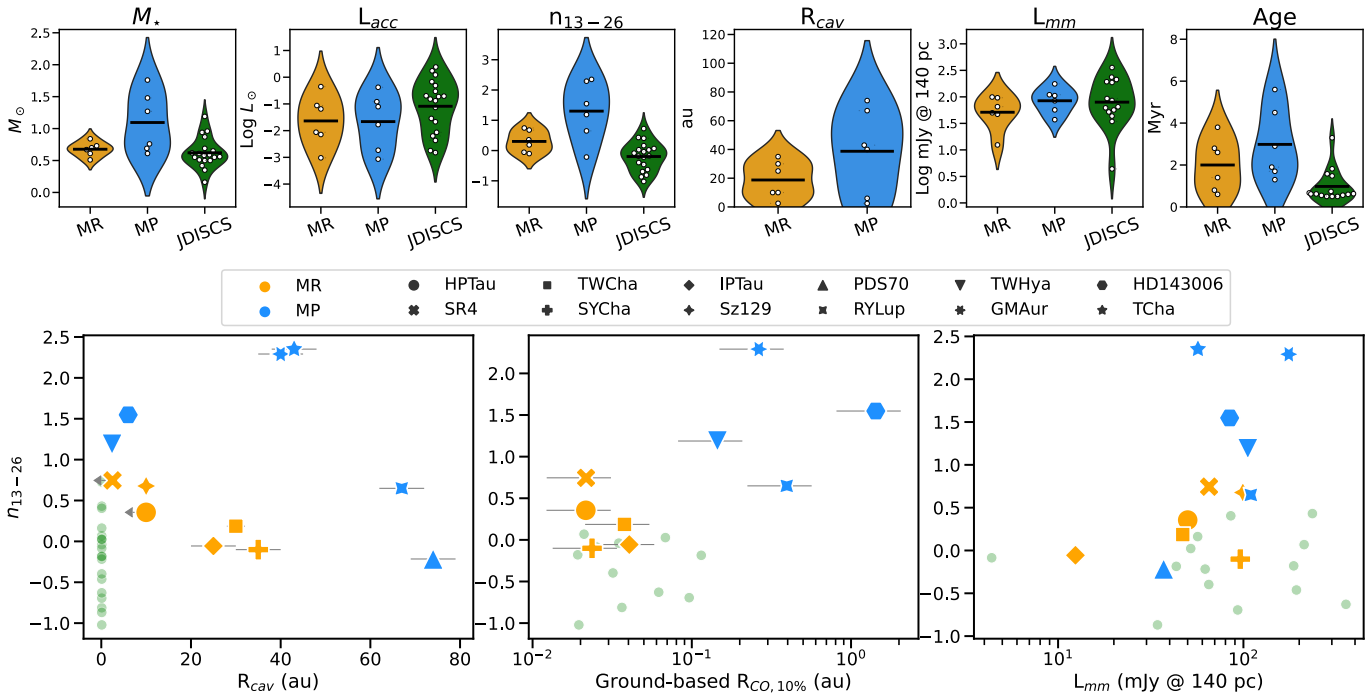

Figure 8. Sample properties for disks with cavities included in this work. Disks with cavities are separated into "molecule rich" (MR, orange) and "molecule poor" (MP, blue) as explained in Section 3. The reference sample shown in green is the JDISCS-C1 sample (Section 3.1), assuming $R_{\rm cav} = 0$. $R_{\rm cav}$ is the millimeter dust emission cavity size. Top row: violin diagrams showing individual disks as white dots in each distribution. Bottom row: $R_{\rm CO,10\%}$ is the Keplerian radius of near-infrared spectrally resolved CO emission at 10% of the line peak, tracing high-velocity molecular gas from ground-based observations (Table 1).

emission is not observed, indicating that CO gas has receded to >0.1–1 au (bottom middle panel in Figure 8). This clear separation in CO emitting radius shows that the molecular dichotomy observed in disk cavities in this work has a radial evolution component to it, where molecules in MP cavities must be strongly reduced in an inner region that is instead rich in molecules in full disks and MR cavities.

To summarize, the MR/MP molecular dichotomy in dust cavities does not seem to be primarily due to large differences in stellar or accretion luminosity, nor distinguished by the size of the millimeter cavity or the disk dust mass (if proportional to the millimeter luminosity). Bearing in mind the relatively small sample size, the main differences emerging between MR and MP in terms of any properties other than the MIRI molecular emission analyzed in this work are (Table 1 and Figure 8):

1. MR are confined within $-0.2 \lesssim n_{13-26} \lesssim 0.75$ and are a mix of IR, mm, and mm+IR dust cavities, while MP typically have $n_{13-26} > 0$, and they are all mm+IR dust cavities (with the exception of PDS 70);
2. the velocity-resolved CO lines indicate narrower lines in MP, showing that the higher-velocity, hotter, inner molecular gas has been depleted;
3. MP include (but are not limited to) supersolar mass stars and larger millimeter dust cavities;
4. MP cavities may also be on-average older than MR cavities, with mean ages of ∼3 Myr versus ∼2 Myr, respectively.

We also note that the two cavity types are not distinguished by the prominence nor the shape of the 10 μm silicate feature (see Appendix A). This feature is being analyzed in a sample that partly overlaps with this work in C. E. Romero-Mirza et al. (2025, in preparation), where the nondetection of water across the entire MIRI spectrum is found in a few disks that consistently show a very weak silicate feature. This is consistent with what is observed in this sample in the only two disks where H_2O is not detected at any wavelength (HD 143006 and T Cha), which may represent the most extreme cases of MP cavities with the least residual inner disk dust within the millimeter cavity.

4.2. Dust Cavity Types and Dust Filtration

The lower IR indices in MR cavities (which extend into slightly negative values consistent with full disks), together with the velocity-resolved CO lines demonstrating molecular gas at <0.1 au, indicate that MR cavities have substantial residual sub-μm dust and molecular gas in an inner region that is instead more depleted in MP cavities. Building on suggestions made in previous analyses of IR spectra (J. R. Najita et al. 2010; C. Salyk et al. 2015, 2019; A. Banzatti et al. 2017; and Section 1), these results support a key role for dust filtration through a millimeter cavity (e.g., W. K. M. Rice et al. 2006; Z. Zhu et al. 2012) in sustaining a rich molecular gas chemistry in the planet-forming region. (Sub)μm-size dust flowing into a millimeter cavity through the cavity edge, where instead millimeter grains are trapped, should in fact sustain molecule formation from H_2, which most easily forms on dust grains (e.g., A. E. Glassgold et al. 2009), as well as shield them from photodissociation (T. Bethell & E. Bergin 2009; S. Bruderer 2013). The role of dust in sustaining molecule formation as well as in shielding them from UV dissociation most likely explains how MR cavities retain spectra that have molecular luminosity more similar to full disks than what is observed in MP cavities.

The residual dust inside the millimeter cavity could be in the form of a radially narrow dust belt with a gap between the

millimeter-cavity edge at larger radii (the case of so-called "pretransitional," hereafter PTD, disks, C. Espaillat et al. 2007; see also Appendix D) or diffuse within the cavity perhaps as streamers (S. E. Dodson-Robinson & C. Salyk 2011), geometries that may vary in different disks and are only in some cases directly resolved (e.g., the case of the inner dust belt in DoAr 44, J. Bouvier et al. 2020). Regardless of the specific geometry, the general emerging picture is that millimeter cavities that still retain enough inner dust to have a similar IR slope to full disks are of MR type while millimeter +IR cavities are of MP type, with some exceptions. The case of MR cavities in particular seems to show a mix of situations with IR-only, millimeter-only, and millimeter+IR cavities in this sample (Table 1), while the only exception in MP cavities is PDS 70 (discussed in Appendix D). Future samples will be fundamental to confirm the distribution in each type (see Section 4.6), and dust modeling work should be done to understand the bifurcation of dust cavities in Figure 8.

We remark that the weaker line luminosity measured in MP cavities argues against dust evolution simply through growth and settling in these disks. Dust settling is expected to increase the line luminosity of all molecules by removing small dust grains from the disk surface over time, lowering the dust opacity, and therefore increasing the visible column of molecular gas (A. J. Greenwood et al. 2019) that can, at high enough densities, self-shield from UV dissociation (e.g., T. Bethell & E. Bergin 2009; S. Bruderer 2013; J. Kanwar et al. 2026). At least some gas density depletion seems therefore to be necessary to explain at least the MP cavities, as we will discuss more in the next sections. The correlations between molecular luminosities and n_{13-26} in Figure 4, instead, seem to support the role of dust settling in the atmosphere of full disks: if more negative n_{13-26} values are truly driven by higher levels of dust settling (P. D'Alessio et al. 2006; E. Furlan et al. 2009), this could explain the increase in line luminosity as explained above based on A. J. Greenwood et al. (2019). The range in line luminosity in full disks may therefore be regulated by dust settling producing $-1 \lesssim n_{13-26} \lesssim 0$, while $n_{13-26} \gtrsim 0$ may predominantly reflect dust depletion in the form of a cavity. New dedicated dust model grids are necessary to test the interpretation of all these trends.

4.3. Gas Density in Disk Cavities

While molecular spectra of MP cavities are clearly subluminous, even those of MR cavities show a few remarkable differences from those of full disks. Organic emission, particularly from C_2H_2, is overall subluminous (Figure 3). A similar drop in luminosity is observed in the CO $v = 2$–1 lines and, to a lesser extent, in the H_2O $v = 1$–1 lines (Figure 3). Moreover, a line ratio identified in previous work as being sensitive to the H_2O column density in the warm-hot reservoir (A. Banzatti et al. 2025; D. Gasman et al. 2025) shows values consistent with a decreased column density in the emitting layer, by a factor of 10 (or more) than in full disks (middle plot in Figure 5). To support that, the OH/H_2O ratio increases in MR cavities in comparison to full disks (Figure 7), which could be due to an increase in H_2O photodissociation by UV. A lower column density of H_2O provides a potential important clue for the interpretation for the subluminous C_2H_2 emission in terms of a lower gas density in the emitting layer, as we will discuss in the following.

To further investigate any evidence for a lower gas density, we consider two additional independent tracers that are covered in MIRI spectra: the excitation of higher-vibrational lines of CO $v = 2$–1 and H_2O $v = 1$–1 lines relative to their lower vibrational levels, which due to the different critical densities (higher in higher-vibrational levels) are sensitive to the gas volume density in the emitting layer. This has been previously discussed in thermochemical models of non-LTE excitation of rovibrational CO lines observed in disks (e.g., S. Bruderer 2013; W. F. Thi et al. 2013; J. Kanwar et al. 2026), finding that CO is generally excited in non-LTE and that the CO $v = 2$–1/$v = 1$–0 ratio decreases with both the CO volume density and column density due to an increasing deviation from LTE in lower-density gas (Figure 4 in A. D. Bosman et al. 2019). For water, a similar effect is expected in the relative excitation of lines from $v = 1$ in comparison to $v = 0$, where the subthermal excitation of the former is due to deviation from LTE as the gas density decreases from the critical density of these transitions (R. Meijerink et al. 2009; A. D. Bosman et al. 2022). Both the $v = 1$–0 and $v = 1$–1 lines of water observed with MIRI have been confirmed to be excited in non-LTE, suggesting a gas density of $<<10^{13}$ cm^{-3} in the emitting layer (see Figure 7 and its discussion in A. Banzatti et al. 2025).

We show the CO $v = 2$–1/$v = 1$–0 and H_2O $v = 1$–1/$v = 0$–0 ratios measured in this work in Figure 9. The lines used in the ratios are the same as shown in Figure 3, where for the H_2O $v = 0$–0 line we use the hot component that has similar upper level energy as the H_2O $v = 1$–1 line ($E_u = 6000$ K). Both these ratios on-average decrease in MR cavities in comparison to full disks, suggesting that indeed the gas density is lower and supporting the lower column density suggested by the $v = 0$–0 line ratio in Figure 5. The deviation between full disks and cavity disks is much more prominent in the CO ratio than in the H_2O ratio; while the MR cavity sample needs to be increased to better assess its distribution, a larger deviation from LTE excitation in the CO $v = 2$–1 lines may be due to their higher critical density ($\gtrsim 10^{13}$ cm^{-3}, W. F. Thi et al. 2013; P. Woitke et al. 2016; J. Kanwar et al. 2026).

Three independent lines of evidence in MIRI spectra therefore point toward a decreased gas density in the emitting layer in disk cavities: the flux ratio of H_2O $v = 0$–0 lines that have different Einstein-A coefficient, and the subthermal excitation of CO $v = 2$–1 lines, and, to a lesser extent, the H_2O $v = 1$–1 lines. The confirmation of this interpretation for the line ratios requires dedicated thermochemical modeling applied to inner disk dust cavities, which so far has mostly been applied to the pure rotational lines of CO (S. Bruderer 2013). We remark that a lower gas surface density may already be implied by the lower accretion rates measured in disk cavities (Figures 2 and 8; and J. R. Najita et al. 2007), which in this case would imply that the lower density is not just in the emitting layer observed with MIRI but in the accretion region and possibly the inner disk itself. A lower emitting gas mass in inner disk cavities in comparison to full disks has indeed been found from fits to rovibrational CO spectra (C. Salyk et al. 2011a; A. Banzatti et al. 2015) and to rotational H_2O emission (C. E. Romero-Mirza et al. 2025, in preparation). A lower density could also provide an explanation for the more prominent cold water emission in cavity disks on average in comparison to full disks, both in the 1500/3600 K and 1500/6000 K ratios and in the 1448/1615 K ratio (Figures 5 and 6).

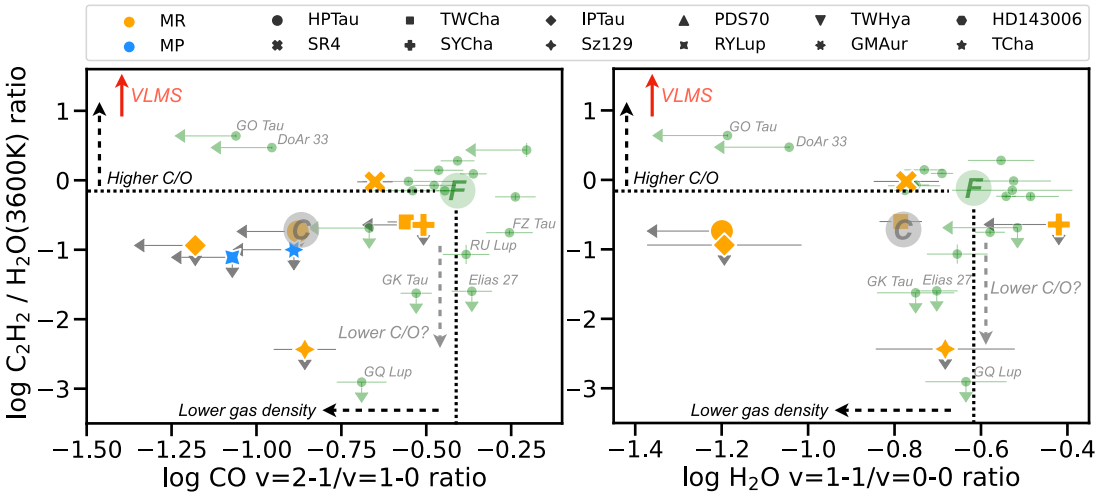

Figure 9. Line flux ratio diagram for C_2H_2/H_2O, sensitive to the elemental C/O ratio, and the vibrational ratios for CO (left) and H_2O (right), sensitive to the gas density (see Section 4.3 for a discussion of their interpretation). Median values are shown by the larger circle marked with "*C*" for cavities and "*F*" for full disks; the latter is used for reference to identify the suggested interpretation of this diagram in terms of a higher C/O (on the top) versus a lower gas density (on the left). Some T Tauri disks are consistent with a lower gas density and yet show a higher C_2H_2/H_2O ratio, DoAr 33 and GO Tau; thermochemical modeling found evidence for an increased C/O ratio in at least one of them (M. J. Colmenares et al. 2024). The red arrow shows the region of very-low-mass stars (VLMS), which are found to have even higher C_2H_2/H_2O ratios as indicative of their supersolar C/O ratio (A. M. Arabhavi et al. 2025; S. L. Grant et al. 2025). Other disks at the opposite corner of the diagram might be due to a lower C/O ratio in the emitting layer (see text for details).

While an increased pebble drift is proposed to explain increased cold emission in full disks (A. Banzatti et al. 2023; S. Krijt et al. 2025), a decreased hot-warm gas density may expose more prominently the colder emission closer to the midplane snowline in cavity disks, especially in MP cavities. Another potential explanation is that the water spectrum in disk cavities may simply look colder due to a larger deviation from LTE (M. Vlasblom et al. 2025), which again could be due to a lower gas density.

The other prominent difference between cavity disks and full disks is that organic emission, especially from C_2H_2, is on-average subluminous not only in MP cavities but also in MR cavities (Figure 3). In Figure 9, we now show the C_2H_2/H_2O ratio, which has become a leading proxy for the elemental C/O ratio as observed with MIRI in inner disks (B. Tabone et al. 2023; M. J. Colmenares et al. 2024; A. M. Arabhavi et al. 2025; S. L. Grant et al. 2025; F. Long et al. 2025), even if these molecules do not necessarily trace the same disk region, especially at high C/O ratios, and therefore, this molecular ratio does not directly trace just the elemental C/O ratio (see J. Kanwar et al. 2026). In the ratio, we use the intermediate energy levels for water to include a few MP cavities in the diagram, those where both CO and water are detected, but we remark that the relative distribution of the other points in the diagram does not significantly change if we use the higher-energy lines of water. Thermochemical models show that the formation of organic molecules is slower than H_2O, and it is driven by X-ray chemistry (e.g., C. Walsh et al. 2015; D. E. Anderson et al. 2021; P. Woitke et al. 2024). Contrary to H_2O, organic emission should become weaker with increasing UV irradiation due to photodissociation that counters the X-ray-induced production (I. Kamp et al. 2017; P. Woitke et al. 2024), in agreement with the disappearance of organic emission during strong UV outbursts (A. Banzatti et al. 2012). If MR cavities have an increased UV penetration into the inner disk due to reduced dust opacity in comparison to full disks, enhanced UV dissociation of organics could in principle explain their weaker emission even if, at high densities, they are expected to self-shield (P. Woitke et al. 2024; J. Kanwar et al. 2026). However, recent models also propose that molecular shielding from dominant oxygen carriers in the upper disk layers should be fundamental to provide additional UV shielding to organics. Some models focused on water in particular, finding the most dramatic difference in C_2H_2 that should be efficiently destroyed and show little to no IR emission when water shielding from UV is absent (S. E. Duval et al. 2022; J. Kanwar et al. 2024). This is strikingly in agreement with the decrease in water column density estimated in MR cavities from $\approx 10^{18}$ to $\approx 10^{17}$ cm^{-2} (Figure 5, middle plot), which is below the efficient UV shielding limit (T. Bethell & E. Bergin 2009). It is also in agreement with the gas density drop suggested by the subthermal excitation of CO $v = 2$–1 and H_2O $v = 1$–1 lines, as discussed above. The gas density is also important for molecule formation, and a density decrease would further limit the formation of organics such as HCN and C_2H_2 to counter their dissociation.

The data in Figure 9 also suggest interesting implications for the elemental C/O ratio in the gas, which strongly affects the relative emission between organics and water (e.g., J. R. Najita et al. 2011; P. Woitke et al. 2018; D. E. Anderson et al. 2021; J. Kanwar et al. 2026). The C/O ratio probably does not increase in disk cavities in comparison to full disks. This can be concluded from comparison to two full disks that show a decreased gas density and yet an unusually strong C_2H_2 feature relative to other molecules: DoAr 33 and GO Tau (their remarkably similar C_2H_2 spectra can be seen in N. Arulanantham et al. 2025). The former was analyzed with thermochemical models in M. J. Colmenares et al. (2024), suggesting that a much higher C/O ratio of 2–4 is necessary to reproduce the strong organic emission relative to water, similarly to what is proposed for VLMS disks that typically show an even higher C_2H_2/H_2O ratio (A. M. Arabhavi et al. 2025; S. L. Grant et al. 2025; J. Kanwar et al. 2026). At the opposite corner of the diagram, a subgroup of full disks seem to be consistent with normal or only slightly reduced gas density and a lower C/O ratio; some of these disks had

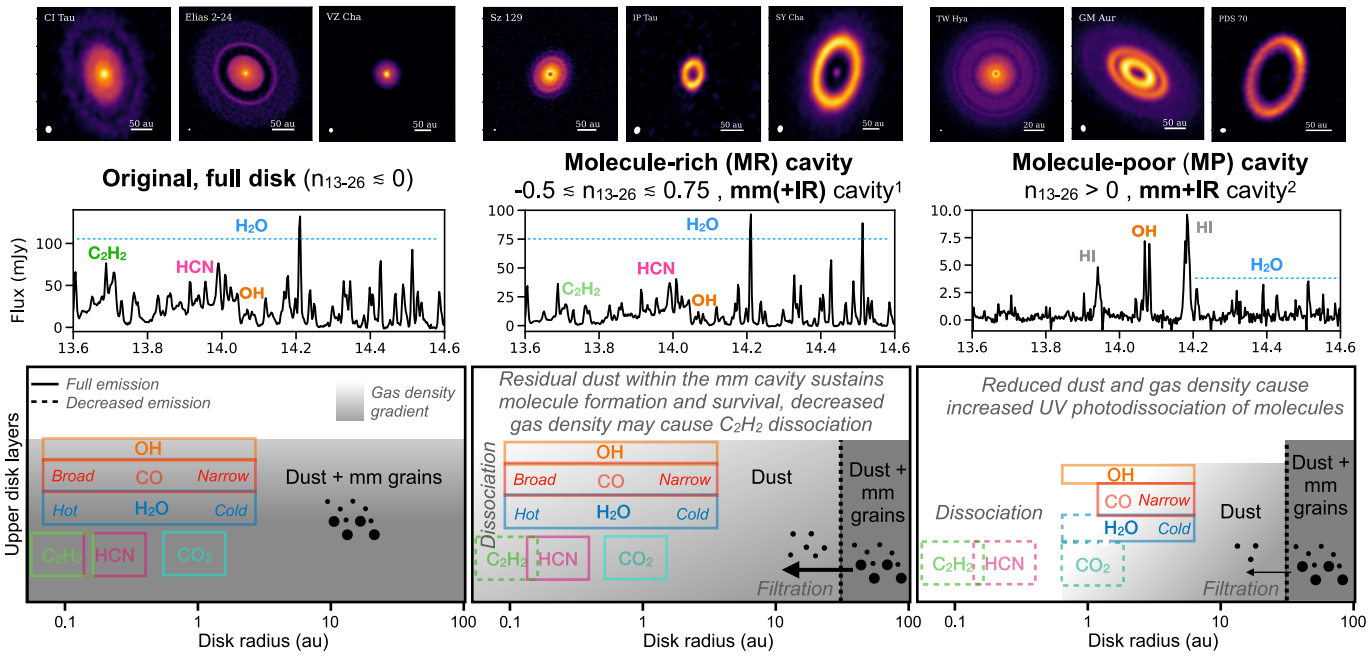

Figure 10. Schematic illustration of the properties and relative distribution of μm-size dust, millimeter grains, and molecular gas in the two cavity types presented in this work in comparison to a full disk (with representative molecular emitting regions adopted from P. Woitke et al. 2024). The illustration includes several simplifications and is not meant to reproduce the exact geometry of the inner disk nor which process is opening the millimeter cavity; see Section 4 for a discussion of each dust and gas component in the different cavity types. Some gradients observed in the data are labeled for reference, including the temperature gradient in H_2O and line-broadening gradient in CO. The reduced C_2H_2 emission in MR cavities is interpreted as due to a decrease in gas density (Figure 9 and Section 4.3). Representative portions of MIRI spectra at 13.6–14.6 μm are included above each disk type for reference; spectra for the entire sample are reported in Appendix A. ALMA continuum images are reported on the top with examples for each disk type (see Section 2.2). Notes: (1) MR cavities are of mixed dust type, but they clearly show a larger IR dust contribution at any millimeter-cavity size (Figure 8); (2) MP cavities are predominantly millimeter+IR dust cavities, with the exception of PDS 70.

dubious broad features under the organics that have been attributed to solid-state emission (N. Arulanantham et al. 2025). It is interesting that two of these disks, GQ Lup and GK Tau, have prominent cold water emission previously attributed to oxygen-enrichment by inward pebble drift in the disk (A. Banzatti et al. 2025; S. Krijt et al. 2025; C. E. Romero-Mirza et al. 2025; M. Vlasblom et al. 2025). The diagram in Figure 9 may become useful in the future to study the effects of the gas density versus C/O ratio to explain organic emission in inner disks in general, not only in disks with a dust cavity. The suggested interpretation of the diagram axes as tracing the C/O ratio and gas density in the emitting layer discussed in this section should be thoroughly investigated with future dedicated thermochemical modeling applied to full disks and cavity disks, which should assess also the effects of changes in temperature and dust opacity in the observable disk layer.

4.4. Dust and Gas Evolution, and Molecule Survival

In Figure 10, we provide a simplified illustration to summarize the relative distribution and evolution of dust, millimeter grains, and molecular gas emerging from this work for MR and MP. For reference, we adopt approximate emitting regions from thermochemical models of a full disk that show a radial and vertical stratification of molecules as observed with MIRI (Figure 11 in P. Woitke et al. 2024) where organics emit from a narrower and hotter inner region while water, CO, and OH come from a higher and more radially extended layer to account for their observed radial gradients. In the figure, we show a potential interpretation of the approximate evolution of those emitting regions to reconcile all the observational results described above in this work.

In an MR cavity, dust filtration through the millimeter cavity (indicated by the lower n_{13-26} index relative to an MP cavity, see Figure 8) may play a key role in sustaining water and CO to similar levels as in full disks, as indicated by the luminosity observed in these molecules (Figure 3). In an MP cavity, instead, the reduced dust (indicated by the higher n_{13-26} index) may lead to a general dissociation of molecules reducing all the hot gas tracers and leaving only a cold residual H_2O layer (see Section 3.2), narrow CO emission, and a persistent layer of OH emission from water photodissociation (see Section 3.3). The gas density may decrease in all cavities and in particular in MP, as suggested by the decrease in luminosity of CO $v = 2$–1 and H_2O $v = 1$–1 lines relative to their lower vibrational lines (Figures 3 and 9), extending the UV photodissociation of molecules down to deeper layers, which could explain the increased OH/H_2O ratio and the drop in C_2H_2 luminosity in both MR and MP cavities (Figures 7 and 9), when molecular shielding from the main oxygen carriers in the upper disk layers is reduced.

4.5. Common Evolution or Different Processes?

Previous work suggested that disks with spatially resolved millimeter dust cavities may be a long-lasting evolutionary phase that happens only in more massive disks (B. Merín et al. 2010; J. E. Owen 2016; P. Pinilla et al. 2018b; N. van der Marel et al. 2018; P. Pinilla et al. 2020), while most disks might evolve to disperse through an "anemic"/"homologously depleted"/"evolved" phase where the SED decreases at all wavelengths without signs of developing an inner dust cavity

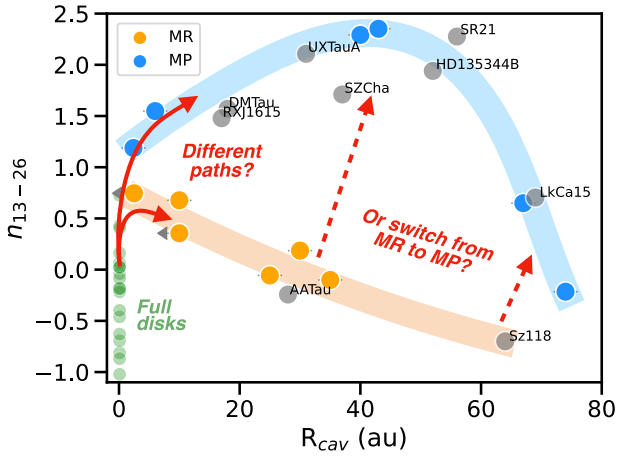

Figure 11. Same as bottom left panel in Figure 8 but marking the two potential interpretations discussed in Figure 10 and in the text. The regions defined by the current samples of MR and MP are highlighted by eye with shaded orange and blue bands, respectively. The gray data points show additional disks observed with MIRI as of Cycle 4 with n_{13-26} measurements available from previous Spitzer spectra.

first (C. J. Lada et al. 2006; J. Hernández et al. 2007; T. Currie & A. Sicilia-Aguilar 2011; L. Ingleby et al. 2011; A. Sicilia-Aguilar et al. 2011). The older age and high millimeter luminosity of cavity disks in this work (Figure 8) do support the idea that at least some of these disks are long-lived and as massive as full disks. Within this general framework, we wish to inquire whether the MR/MP dichotomy may be a sign of sequential rather than different evolutionary paths.

As described above, we find that the MR/MP dichotomy does not relate to the millimeter-cavity size nor accretion onto the star, but it is instead related to a drop in gas density and to the residual content of small ($\lesssim\mu$m) dust grains within the millimeter cavity. A possible evolutionary scenario to reconcile these aspects is that all cavities may at first form as MR, developing from full disks by opening a millimeter cavity at any radius (2–70 au, the range observed in this sample). All these millimeter cavities may at first retain enough μm-size grains, supplied by filtration through the cavity edge, to sustain the formation and survival of molecular gas inside the cavity. As time passes, the μm-size dust mass within the cavity may decrease by an imbalance between stellar accretion or grain growth and dust filtration through the cavity edge (e.g., Z. Zhu et al. 2012). A decrease in inner disk dust in turn increases the observed n_{13-26} index and moves up the disk in Figure 11 to eventually become an MP cavity. In the context of this potential scenario, the small age separation (with MP cavities that are on average $\sim$1 Myr older than MR) is in stark contrast with the net separation of MR and MP in the n_{13-26} versus $R_{\rm cav}$ plane in Figure 8, suggesting that if it is indeed a time evolution it must be rather fast to switch from MR to MP. Perhaps, due to shielding (dust shielding gas, and molecular shielding from CO and H_2O), there is a fast tipping threshold between an MR to an MP surface layer due to dissociation, a threshold that may depend on a specific dust and gas density.

To determine the inner disk structure, it is very important to understand what happens to the dust after its filtration through the millimeter cavity. Using dust evolution models applied to the disk of PDS 70, P. Pinilla et al. (2024) show that dust growth to millimeter grains in the inner 10 au depends on the mass of small dust grains filtering through a pebble trap farther out. As the dust growth timescale is inversely proportional to the dust-to-gas ratio (e.g., T. Birnstiel 2024), if the dust-to-gas mass ratio in the inner disk is reduced and the inner gas mass is kept constant or it decreases in much longer timescales, then the grain growth timescales are much longer. If the dust mass in the inner disk drops below $\sim10^{-4}\,M_\oplus$, recoagulation becomes too slow, and the inner disk contains only $\lesssim$1–10 μm grains (Figures 1 and 2 in P. Pinilla et al. 2024), effectively becoming a millimeter-cavity disk that does not show an IR deficit. Initially, as gas and dust masses are relatively high, it is expected that molecules (e.g., CO, H_2) can readily survive (S. Bruderer 2013), and the millimeter cavity would be of MR type. However, as the gas and dust content in the inner disk dwindles, another transition may take place. Using thermochemical models of disks with gaps and different depletion levels, S. Bruderer (2013) shows that, once the gas mass interior to 10 au drops below $\sim0.2\,M_\oplus$, shielding by residual small dust is needed to allow molecules to survive (Figure 8 and Table 2 in S. Bruderer 2013). Lowering this residual dust mass from $\sim2\times10^{-4}M_\oplus$ to $\sim2\times10^{-9}M_\oplus$ removes this shielding effect and causes a dramatic decrease in the column densities of CO and H_2 (Figure 8 in S. Bruderer 2013), possibly providing a transition from MR to MP.

In summary, previous modeling of dust cavities, while it still needs to be applied to test a transition between MR and MP, can in principle support a sequence of events in which an MR millimeter cavity may form first, and the transition from MR to MP takes place later, with both transitions being triggered by their own inner disk dust (and gas) mass thresholds. This scenario may also explain why cavities around IMTTS (and Herbig) stars are typically MP, if disks around higher-mass stars evolve more rapidly and move to the MP phase earlier.

A possible alternative is that, instead, dust cavities may form from the start as either MR or MP depending on a different cavity-opening process. Given their similar stellar accretion, cavity size, and dust mass as inferred from the millimeter luminosity (Figure 8), the different processes giving an origin to MR rather than MP should act on a similar radial disk region and enable similar accretion onto the star, but differ in the amount of residual μm-size dust within the millimeter cavity and possibly in the gas density as discussed above. Multiple processes have been proposed to form a dust cavity: grain growth and settling, planet dynamical interactions, disk winds, dead zones (e.g., J. R. Najita et al. 2007; C. Espaillat et al. 2014; B. Ercolano & I. Pascucci 2017; N. van der Marel 2023; and references therein). Models including planets of different mass have been particularly successful in explaining bright disks with large cavities that still retain accretion onto the star (K. A. Marsh & M. J. Mahoney 1992; J. R. Najita et al. 2007; S. E. Dodson-Robinson & C. Salyk 2011; S. Huang et al. 2024). The combination of planets or dead zones with MHD or photoevaporative winds has been increasingly successful in explaining a large range of conditions up to larger cavities and higher accretion rates (P. Pinilla et al. 2016; B. Ercolano & I. Pascucci 2017; N. P. Hendler et al. 2018; M. Gárate et al. 2021; É. Martel & G. Lesur 2022). The MR/MP dichotomy provides a new observational ground to investigate these scenarios in future work and determine if the dichotomy in inner disk molecular emission is a proxy for a specific cavity-opening process over another. It is worth noting that recent work using GAIA astrometry proposed a $>20\,M_{\rm jup}$ companion

in T Cha and a $> 50\,M_{\rm jup}$ companion in RY Lup (M. Vioque et al. 2026), which in addition to the known protoplanets in PDS 70 (M. Keppler et al. 2018; S. Y. Haffert et al. 2019) suggests that at least some MP cavities may be produced by massive companions.

4.6. Expanding the Sample

Figure 11 shows again the dichotomy in MR and MP in the IR index versus millimeter-cavity size space emerged from this work (based on Figure 8), and marks the bifurcation into two trends discussed above in this section. In this new figure, we include as gray data points additional cavity disks that have been observed with MIRI in other programs (C. C. Espaillat et al. 2023, 2024; G. Perotti et al. 2025, in preparation; C. E. Romero-Mirza et al. 2025, in preparation) where the IR index can be measured from previous Spitzer data. This larger sample supports the net separation of disk cavities that is emerging from this work in the n_{13-26} versus $R_{\rm cav}$ plane, with a sharp bifurcation into millimeter+IR cavities in the MP branch and MR cavities that for smaller R_{cav} are millimeter +IR cavities too but extend into negative values of n_{13-26} at $R_{cav} \gtrsim 30$ au. Future analyses of larger samples of MIRI spectra will enable testing if the molecular emission follows the two types as predicted here and will better characterize the distribution of properties in the two cavity types, specifically addressing the fundamental questions on their evolution discussed above (including a possible age difference).

Based on cavity disks that have previous Spitzer data, using the n_{13-26} value, we can compile a list of additional disks for each cavity type that could be tested in the future with MIRI spectra (targets with an asterisk have already been observed with MIRI in other programs and are included in Figure 11 using their available Spitzer-based n_{13-26} values):

Predicted MR cavities. These are AA Tau*, Sz 118*, CIDA 1, HP Cha, Sz 100, WSB 60, and RY Tau.

Predicted MP cavities. These are DM Tau*, LkCa 15*, UX Tau A*, SZ Cha*, SR 21*, HD 135344B*, RXJ 1615*, RXJ 1852, CS Cha, V1247 Ori, LkHa 330, CQ Tau, and MWC 758.

4.7. How Can We Identify an Inner Disk Cavity?

As we have discussed in this work, each observable that has been used so far to identify a dust disk cavity has its own limitations (Section 1 and Appendix B). Millimeter cavities can be directly imaged only when larger than the spatial resolution achieved with millimeter interferometers, which in principle means ∼5 au, but often, it is much larger than that. Small (<15 au) dust cavities have therefore mostly been missed in the millimeter surveys obtained so far even with ALMA (N. van der Marel 2023). On the other hand, the IR index n_{13-26} also does not reveal all the inner disk cavities, which can extend well into the negative values that are typically attributed to full disks (Figure 11). The reason why we can clearly identify some cavities in disks with $n_{13-26} < 0$ in this work is that we have a direct detection of the millimeter cavity from ALMA. However, would it be possible to identify a disk with a cavity in absence of a direct detection from ALMA? This question is especially relevant in the case of star-forming regions that lack the highest-resolution ALMA data or that are farther away, especially at kiloparsec distances where the ALMA resolution decreases significantly. These disks are still well observable at the sensitivity of JWST-MIRI (e.g., M. C. Ramírez-Tannus et al. 2025), and IR spectra provide invaluable data to study the evolution of planet-forming regions especially at these distances.

We can use the results of this work to propose specific observables that can be used to identify a disk cavity purely from an MIRI spectrum, assuming an ALMA image is not available or not at a spatial resolution better than ∼40 au. These criteria should be valid for T Tauri disks at ∼0.5–5 Myr around solar-mass stars (0.5–1.3 $M_{\odot}$), as included in this work (Table 1). First of all, $n_{13-26} > 0$ should be a first indicator of a disk cavity (Figure 8), particularly when molecular emission is subluminous in comparison to trends defined by full disks as a function of accretion luminosity (Figure 3). A notable exception can be disks viewed at high inclinations ($\gtrsim$70°), which will decrease the IR flux at shorter wavelengths and increase the n_{13-26} index similarly to an inner cavity (e.g., N. P. Ballering & J. A. Eisner 2019; and Appendix B). However, MR cavities can also have $n_{13-26} < 0$, when enough residual dust is present within the millimeter cavity as discussed above in this work. The bifurcation discovered in Figure 8 now suggests that future work should explore and determine a more suitable way to classify IR cavities based on their SED. In ambiguous cases, MIRI spectra offer a number of other observables that may reflect the depletion of the inner disk: in this work, we have identified in particular that subluminous C_2H_2 and subluminous higher-vibrational-state lines of CO and H_2O (Figure 9) may provide evidence for a decrease in gas density in the hot inner gas, even in disks where the IR index alone does not provide clear evidence for dust depletion. This finding indicates a path for future work to study, in larger samples and dedicated model explorations, the interconnection of dust and gas evolution and the onset of gas depletion in planet-forming regions, with its fundamental implications in planet formation.

5. Summary and Conclusions

Expanding on previous findings from Spitzer and ground-based spectra (J. R. Najita et al. 2010; C. Salyk et al. 2011b, 2015, 2019; A. Banzatti et al. 2017; see Section 1), in this work, we have formally defined two types of T Tauri disk cavities based on their observed IR molecular spectra. We compare the MIRI-MRS measured molecular luminosities to those from full disks as a function of accretion luminosity, which has the strongest correlation with the molecular luminosity in full disks (A. Banzatti et al. 2020, 2025; and Appendix C). "MR" cavities have a molecular luminosity that is generally consistent with that measured in full disks with similar accretion, except in the case of organic molecules that can be subluminous, while "MP" cavities are significantly subluminous in all molecules except in some cases the OH lines.

From the point of view of the solids, these two cavity types are not separated by the millimeter-cavity size $R_{\rm cav}$ (which however extend to larger sizes in MP cavities in this sample) nor the millimeter luminosity (and in turn supposedly the mass). However, we discover a bifurcation with two distinct branches in the n_{13-26} versus millimeter $R_{\rm cav}$ plane indicative of different degrees of depletion in (sub)μm-size dust within the millimeter cavity (Figures 8 and 11): for the same $R_{\rm cav}$, MR cavities have significantly lower n_{13-26} values demonstrating residual dust that can help molecule formation and shielding from UV dissociation. The stark dichotomy and bifurcation in

this diagram are fundamental results from this work that are currently supported by increasing the sample with cavity disks from other programs (Figure 11). The IR n_{13-26} versus millimeter R_{cav} diagram may become an important framework for future studies of the physical and chemical structure of disk cavities and their evolution.

From the point of view of the gas, MR and MP are not separated in accretion luminosity, but the molecular gas shows strong differences (Figure 3). MR cavities have several properties consistent with those observed in full disks: broad CO lines (as velocity resolved from the ground, Figure 8) indicating emission extending to <0.1 au and strong emission from hot molecular gas tracers (including high-energy H_2O and CO). However, organic emission tends to be subluminous, especially in C_2H_2, and water is consistent with a ~10 times lower column density and is dominated by colder emission, confirming and expanding earlier evidence that emerged from Spitzer and ground-based spectra (see above). A new discovery of this work is that all T Tauri disks with a cavity have subluminous CO $v = 2$–1 and, to a lesser extent, H_2O $v = 1$–1 lines, suggesting further deviation from LTE excitation as due to a decrease in gas volume density in the emitting layer (Figure 9). Together with the on-average lower stellar accretion in comparison to full disks (Figures 2 and 8), multiple lines of evidence therefore suggest a decreased gas density in inner disk cavities, including in MR cavities. Additionally, MP cavities have narrow CO line profiles indicating the emission has receded to >0.1–1 au and have subluminous emission from all hot gas tracers except OH. Water is not detected in the hotter reservoir typically observed in full disks, and is characterized by temperature profiles dominated by emission at 170–400 K, where detected. Two disks in this sample (T Cha and HD 143006) show the extreme case of MP cavities with nondetection of water at all MIRI wavelengths and weaker 10 μm silicate emission, consistent with findings from C. E. Romero-Mirza et al. (2025, in preparation). These extreme conditions are probably reached by all MP cavities with time, and may be more common at later stellar ages.

The OH emission stands in contrast with other hot molecules by showing a general persistence in disk cavities in transitions across all upper level energies (900–40,000 K), indicative of a persistent H_2O-photodissociation layer as well as possibly different reservoirs down to a collisionally dominated colder layer. Compared to full disks, the measured OH/H_2O ratios across energy levels increase in MR cavities and even more in MP cavities (Figure 7), suggesting an increase in water photodissociation possibly connected to the decrease in gas density (Section 4.3). Put together, the IR molecular emission observed in disk cavities suggests a feedback where lowered dust within a millimeter cavity enhances water photodissociation from a hotter layer first out to a colder layer later; in turn, water dissociation decreases its column density and may additionally enhance the organic destruction rates beyond that driven by the loss of small dust grains. Molecular shielding by H_2O may be particularly important for organic survival in addition to dust shielding and could explain the decrease in organic emission in MR cavities that show evidence for a decrease in gas density, especially in the case of C_2H_2 as proposed in recent models (S. E. Duval et al. 2022). This interpretation should be tested with future thermochemical modeling studies that explore how molecular abundances may vary in full disks and in inner disk cavities under a range of dust and gas depletion factors and a range of elemental C/O ratios, to reproduce different conditions that the distribution of disks in the diagram in Figure 9 may reflect.

As discussed in Section 4, the MR/MP dichotomy could be due to different physical conditions in cavity-opening processes that produce different levels of dust and gas depletion early on and lead to the bifurcation in Figure 11, or to a common evolution where cavities first form as MR and then switch to MP. The net separation in the n_{13-26} versus R_{cav} plane suggests that, if it is part of the same evolution, the switch from MR to MP may happen rapidly and depend on a tipping point across a threshold in dust and gas density. While the limited sample included in this work starts to reveal emerging properties for each cavity type, it will be fundamental to expand the sample to better characterize the typical properties and distribution of each type and their origin in connection to disk evolution and planet formation.

Acknowledgments

The authors acknowledge feedback from an anonymous referee who helped significantly improve the discussion of organics, as well as helpful discussions on the topic with Jayatee Kanwar. The authors are thankful to Marissa Vlasblom for providing new model line fluxes for comparison to the data in Figure 18, and to Joshua Sendgikoski for help with stellar age estimates. This work is based on observations made with the NASA/ ESA/CSA James Webb Space Telescope. The JWST data used in this paper were obtained from the Mikulski Archive for Space Telescopes (MAST) at the Space Telescope Science Institute and can be accessed via: doi: 10.17909/4gpn-y657. The data were obtained from the Mikulski Archive for Space Telescopes at the Space Telescope Science Institute, which is operated by the Association of Universities for Research in Astronomy, Inc., under NASA contract NAS 5-03127 for JWST. The observations are associated with JWST GO Cycle 1 and 2 programs 1282, 1549, 1584, 1640, 2025, 2260, 3228.

Part of this research was carried out at the Jet Propulsion Laboratory, California Institute of Technology, under a contract with the National Aeronautics and Space Administration (80NM0018D0004). The authors acknowledge support from NASA/Space Telescope Science Institute grants: JWST-GO-01640 and JWST-GO-01584. S.K. and T.K. acknowledge support from STFC grant ST/Y002415/1. B.T. acknowledges support by the Programme National PCMI of CNRS/INSU with INC/INP cofunded by CEA and CNES.

Facility: JWST.

Software: Matplotlib (J. D. Hunter 2007), NumPy (S. van der Walt et al. 2011), SciPy (P. Virtanen et al. 2020), Seaborn (M. Waskom 2021), Astropy (Astropy Collaboration et al. 2013, 2018, 2022), LMFIT (M. Newville et al. 2014), iSLAT (E. G. Jellison et al. 2024; M. Johnson et al. 2024).

Appendix A
Additional Figures for the Entire Sample

Figure 12 shows the complete MIRI-MRS spectra of the cavity disks included in this work, with the continuum marked in red for reference (this is the continuum that is subtracted before the analysis of gas emission). Figures 13 and 14 show portions of the continuum-subtracted spectra separated into MR and MP to illustrate their different molecular emission as described and discussed above in this work.

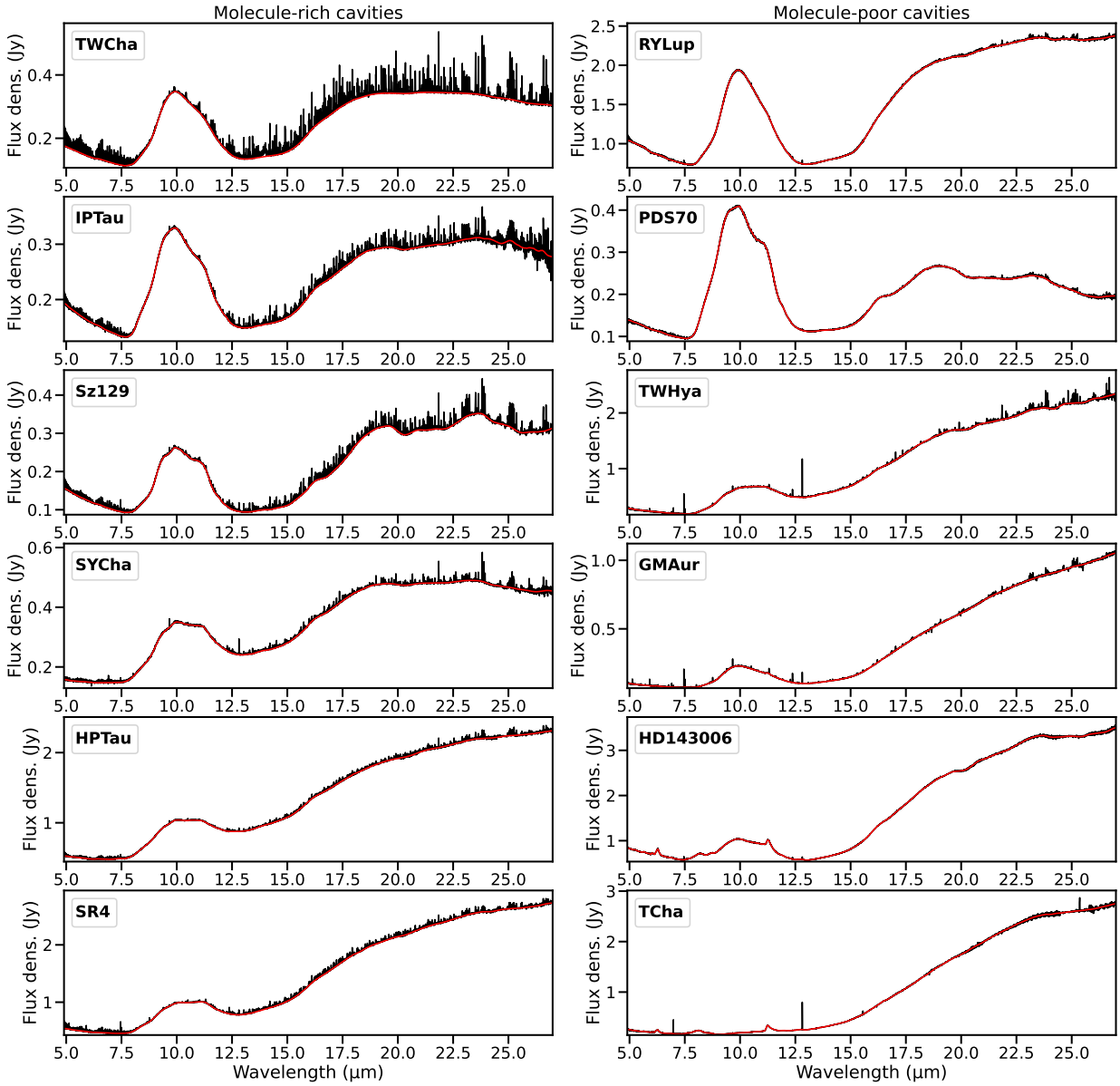

Figure 12. MIRI-MRS spectra for the cavity disks included in this work, with estimated continuum for each one marked in red. The MR/MP dichotomy does not seem to be related to different dust properties as visible in the 10 μm feature shape or prominence.

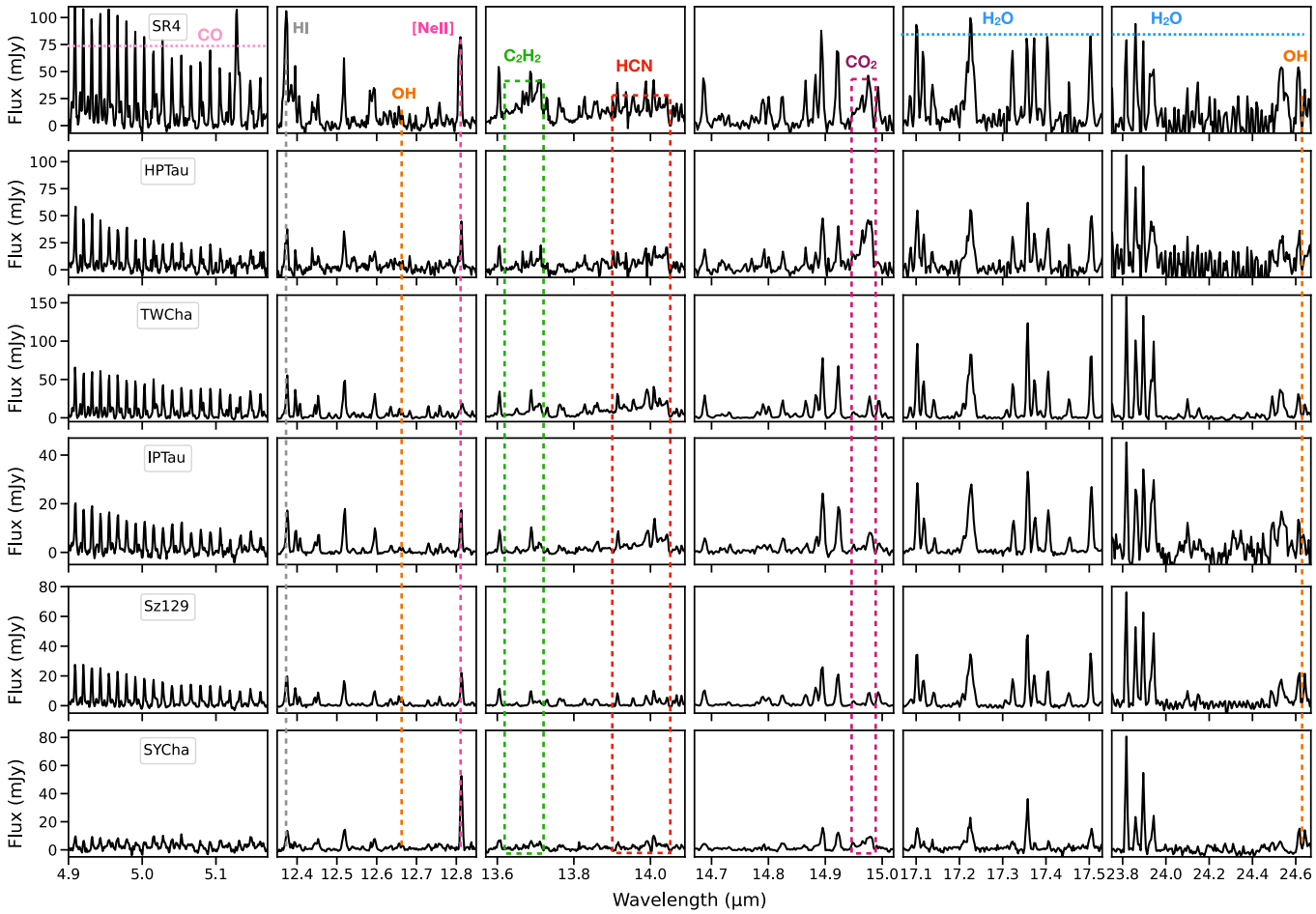

Figure 13. Continuum-subtracted MIRI spectra of MR cavities, showing prominent emission from all the typical molecules and atoms detected at infrared wavelengths in T Tauri disks. Organic emission tends to be subluminous, as shown in Figure 3.

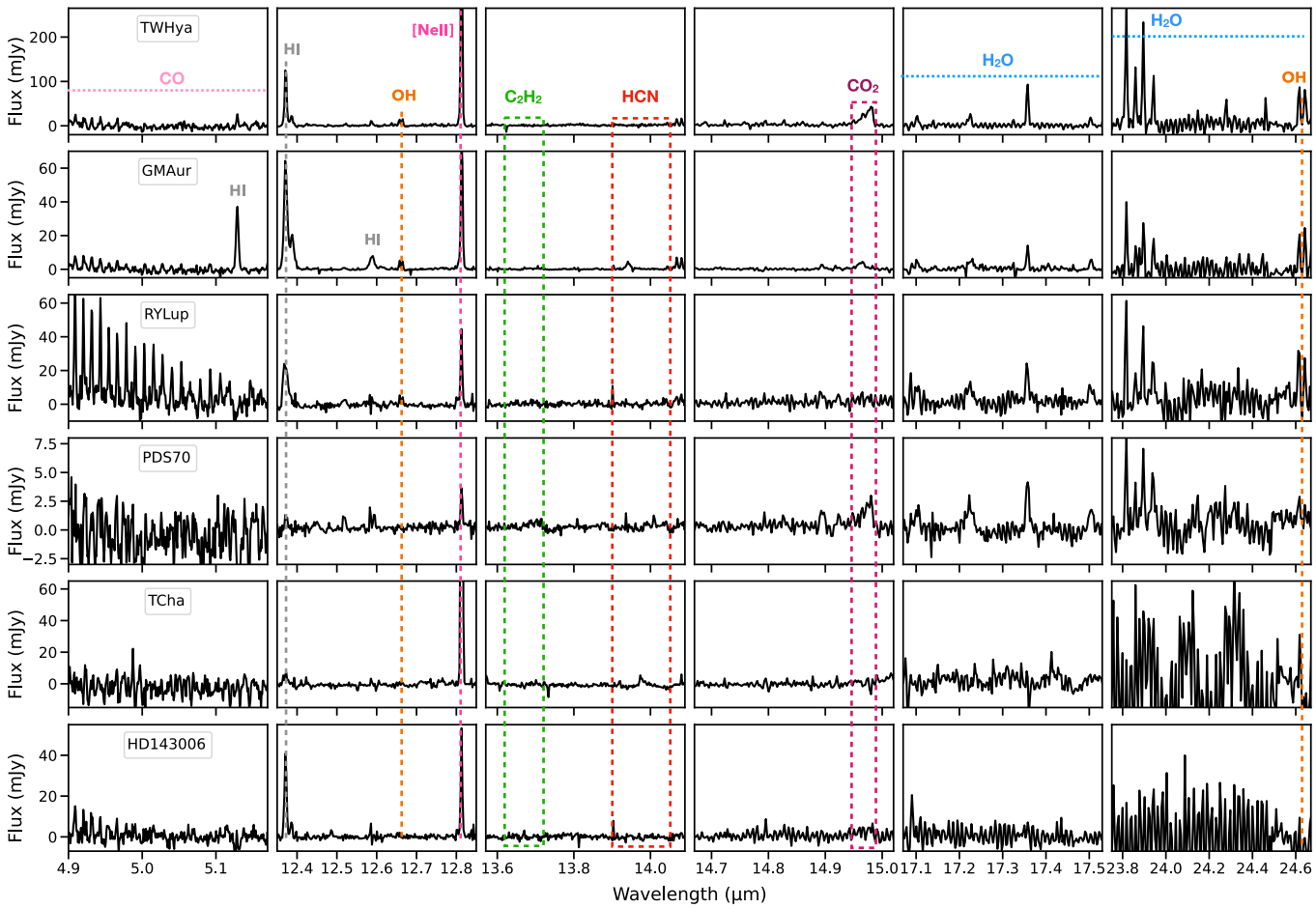

Figure 14. Continuum-subtracted MIRI spectra of MP cavities, showing prominent emission from H I and [Ne II] and residual emission from CO, cold water, CO_2, and OH (not detected in T Cha and HD 143006).

Appendix B
The Infrared Index as a Tracer of a Dust Cavity

With the first studies of inner dust cavities being based on spatially unresolved SED observations and the detection of a deficit at NIR wavelengths followed by an upturn in the far-IR, the slope of the SED at NIR and mid-IR wavelengths has long been used as a proxy to detect the depletion of small dust grains in inner disks (Section 1). We briefly summarize in this section how different IR indices have been used in the past and compare them to the new n_{13-26} index measured from MIRI. We remark, however, that the introduction of these indices based on SED modeling explorations still dates back to works preceding the revolution provided by spatially resolved millimeter interferometry imaging (see references in Section 1; and review by N. van der Marel 2023). Due to the different radial distribution of μm dust versus millimeter grains, SED-based identifications of dust cavities pre-ALMA missed several (large) cavities that are now spatially resolved and known (Section 1). An updated modeling exploration of different IR indices in the context of different dust evolution effects (growth, settling, pebble drift, dust filtration through the millimeter cavity, inner rim structures, and especially the relative depletion of smaller versus larger grains) is long due and should be done in future work.

While multiple spectral indices at wavelengths covered by Spitzer (5–37 μm) were explored, the n_{13-30} ended up becoming the most used to detect an inner dust cavity (E. Furlan et al. 2006, 2009, 2011; J. M. Brown et al. 2007). These previous works determined that radially continuous, optically thick disk structures should have at most $n_{13-30} \lesssim 1$ in typical ISM dust/gas ratio (DGR) conditions (1:100) and found that most disks have instead $n_{13-30} \lesssim 0$, which they proposed to be ubiquitous evidence for dust settling in disk upper layers reducing DGR by factors of 10 to 1000 compared to ISM (P. D'Alessio et al. 2006). Based on that, these works adopted a conservative limit of $n_{13-30} > 1$ to identify large dust cavities, with support from the first spatially resolved images from millimeter interferometers where large dust cavities indeed had $n_{13-30} \gtrsim 1$. Multiple degeneracies affected SED modeling, and a number of "outliers" could not be explained by dust settling, down to $n_{13-30} \sim 0$ and in some cases even below (P. D'Alessio et al. 2006; E. Furlan et al. 2006, 2009). It should be noted that, in these first studies, $0 \lesssim n_{13-30} \lesssim 1$ could only be reproduced with no or little dust settling, implying close to ISM values for the DGR that have later been argued against based on the excitation of IR molecular spectra (e.g., R. Meijerink et al. 2009; A. J. Greenwood et al. 2019). With more SMA and ALMA observations, several millimeter cavities now demonstrate that the n_{13-30} index can indeed be as small as 0, and sometimes lower, even in the case of very large millimeter cavities and even though it does not correlate simply with the size of the cavity at millimeter wavelengths (Appendix D in A. Banzatti et al. 2020).

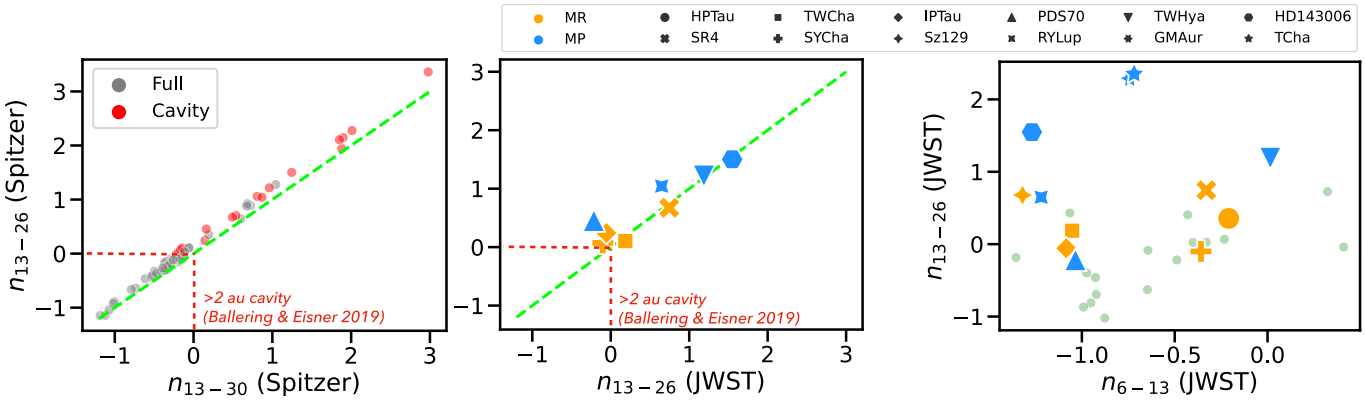

Figure 15. Comparison between different IR index definitions in Spitzer and JWST spectra and detection limits for dust cavities. The green dashed line shows the 1:1 relation. Left: Spitzer sample from Figure 9 in A. Banzatti et al. (2020), with spatially resolved millimeter continuum cavities marked in red. Some disks marked as "full" may have spatially unresolved cavities. For reference, disk models with indices $\gtrsim$0 correspond to inner cavities of size $\gtrsim$2 au in N. P. Ballering & J. A. Eisner (2019). Middle: sample from this work, where in common with the sample in A. Banzatti et al. (2020). Right: MIRI-based n_{13-26} index versus n_{6-13} index for comparison to Figure 11 in E. Furlan et al. (2006). A potential bifurcation unrelated to the MR/MP dichotomy (which are mixed in this plot) may be emerging in the sample in this plot and should be tested with larger samples in future work.

However, the index is also affected by other parameters including the disk inclination angle along the line of sight (e.g., P. D'Alessio et al. 2006; N. P. Ballering & J. A. Eisner 2019; N. van der Marel et al. 2022), which at high viewing angles ($\gtrsim$70) can obscure the inner hot disk region and mimick a dust cavity in the SED. For this reason, in this work, three disks that do not have a dust cavity detected from a millimeter dust continuum with ALMA but have a positive IR index are excluded from the cavity sample due to their high inclination of $\sim$70°, and they are included in the reference JDISCS-C1 sample used in this work (DoAr 25, MY Lup, and IRAS 04385-2550). One of them, MY Lup, has recently been presented and discussed in C. Salyk et al. (2025) in the context of its peculiar molecular emission as possibly due to its high viewing angle or potentially an unresolved small inner cavity. With multiple degeneracies and the possibility of different radial segregation of smaller versus larger dust grains (Section 1), it is expected that a clear cut in n_{13-26} values may not be found to detect an inner dust cavity just from the SED. Based on the index values measured in spatially resolved millimeter cavities, we have decided to adopt a limit of $n_{13-26} \gtrsim 0$ to identify an IR cavity from the SED (A. Banzatti et al. 2020). IP Tau is an example of a case at the boundary, and we indicate its cavity as mm(+IR) in Table 1 to reflect this uncertainty. Given the bifurcation discovered in Figure 8, it seems necessary in future work to explore and determine a more suitable way to classify IR cavities based on their SED.

Figure 15 illustrates how the MIRI-based IR index n_{13-26}, measured at 13.095–13.113 μm and 26.3–26.4 μm where molecular emission is minimal as determined in A. Banzatti et al. (2025), compares to the previously used n_{13-30} from Spitzer. The two indices differ only slightly (with n_{13-26} larger than n_{13-30}) when measured in the same spectrum (left plot in Figure 15), showing that spatially resolved millimeter dust continuum cavities are still indicated by positive values of the n_{13-26}, as it was for n_{13-30}. The n_{13-25} index in E. Furlan et al. (2006, 2009) should be comparable to the new MIRI-based n_{13-26} (we do not use the range at 25 μm due to a cluster of strong water and OH lines, see, e.g., A. Banzatti et al. 2025). We include also the n_{6-13} index used in E. Furlan et al. (2006), which in MIRI we measure at 6.12–6.14 μm where there is a gap in molecular emission (A. Banzatti et al. 2025).

When comparing the n_{13-26} index value as measured from MIRI to that previously measured in Spitzer spectra for the disks where both are available (middle plot in Figure 15), there is some evidence for variability in the SED, especially in the case of RY Lup and PDS 70 (the latter already reported in G. Perotti et al. 2023). We remark that the updated flux calibration in JDISCS reduction 9.0 has significantly changed all the n_{13-26} index values previously measured in reduction version 8.0 and published in N. Arulanantham et al. (2025); in this work, we have used the new values, and we include those measured in the JDISCS-C1 sample in Table 5.

Appendix C
Spectral Ranges and Molecular Measurements

Figure 16 shows all the spectral ranges used to measure line luminosities in this work. The H_2O, CO, and some OH lines are directly taken from the line list provided in A. Banzatti et al. (2025), available in iSLAT as "MIRI_general."[23] This line list was carefully selected by accounting for emission from all the typical molecules observed with MIRI in TTauri disks, to minimize the contamination of each tracer from other species. Using the same contamination-minimization procedure, in this work, we expand that line list with additional OH lines, and we include emission from organics too. The general strategy for all molecules is to use uncontaminated lines that can be directly measured in the MIRI spectra without being impacted by the uncertainties and degeneracies of molecular slab modeling. All molecular spectra and contamination are carefully checked with iSLAT (E. G. Jellison et al. 2024), which enables an inspection of the individual transitions producing the emission from any molecules using data from HITRAN (I. E. Gordon et al. 2022). We remark that, as in A. Banzatti et al. (2025), we included also the H_2O HITEMP line list (L. S. Rothman et al. 2010) that is more complete to check for contamination from high-energy H_2O lines, especially at <18 μm. The line list used in this work should therefore be straightforward to measure and reproduce in any other samples in the future, except for CO_2 where some correction is needed (see below). For measuring emission line properties from the spectra, we use iSLAT, which implements

[23] https://github.com/spexod/iSLAT

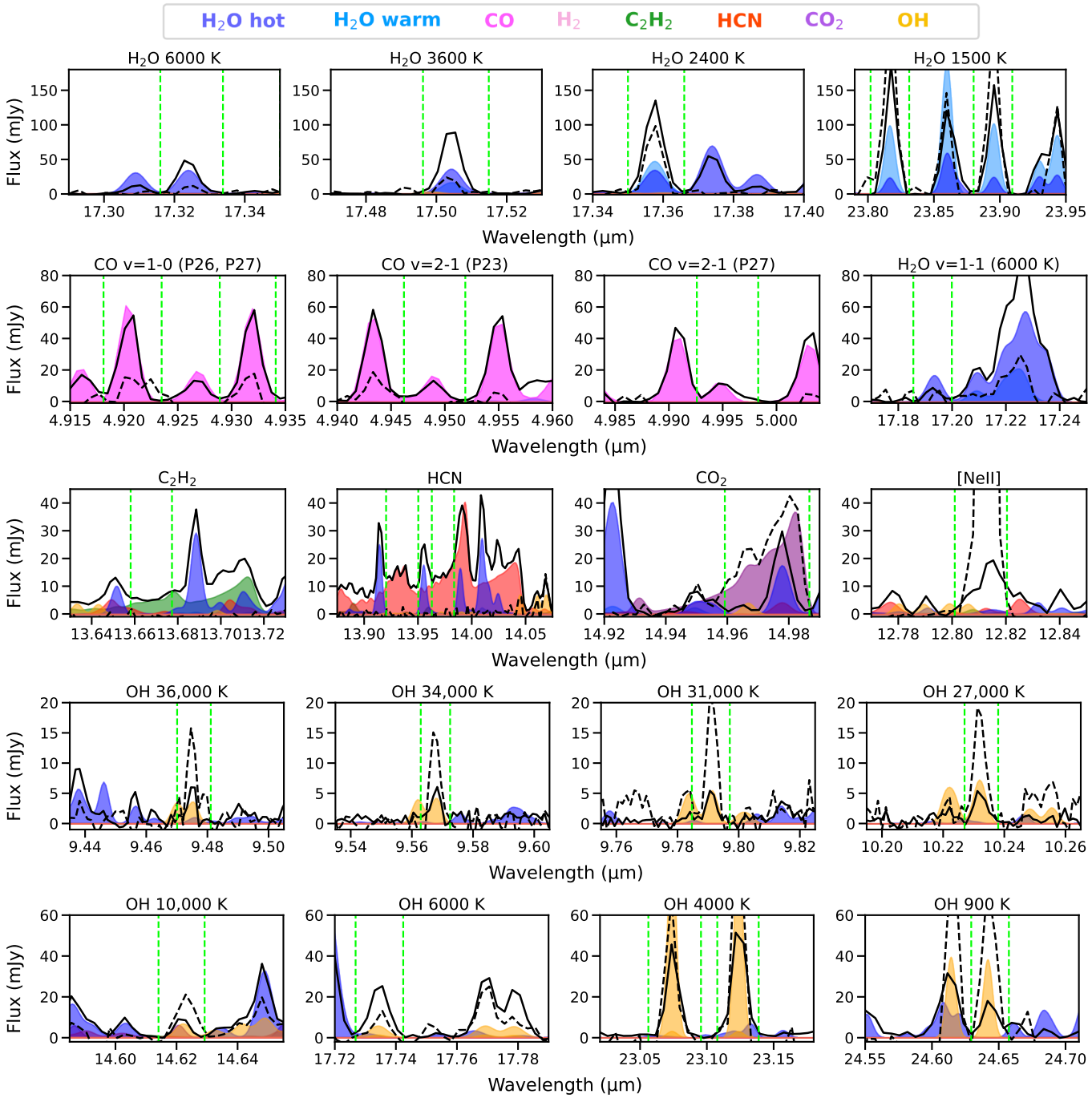

Figure 16. Spectral ranges used for line luminosity measurements in this work (see Table 3), based on A. Banzatti et al. (2025) to determine lines that are free from blending (see Appendix C). The MIRI spectra of TW Cha (solid line) and TW Hya (dashed line) are shown as examples of a molecule-rich (MR) and molecule-poor (MP) disk cavity, respectively. Representative slab models from iSLAT (E. G. Jellison et al. 2024) are shown in each plot for comparison to the data. Vertical dashed lines show the range used to integrate the line flux in each case.

the least-square minimization code `lmfit` (M. Newville et al. 2014) to perform single-Gaussian fits and measure the line flux and uncertainty for individual transitions, while we simply integrate the flux over a specific range in the case of the blended emission from the organics. Table 2 reports detections for all these gas tracers in this sample, Table 3 reports linear regression results for Figures 3 and 4, using the `linregress` function in scipy (P. Virtanen et al. 2020), and Tables 4 and 5 report the line flux measurements and errors for the entire sample of cavity and full disks.

For OH, we select lines across energy levels by careful consideration for blending with other molecules, especially H_2O. All the lines we select are free from contamination except for the 10,000 K line near 14.62 μm, which is contaminated by CO_2 only in cases of relatively stronger emission from this molecule (which are rare in the sample included in this work, see N. Arulanantham et al. 2025). In the disk with strongest relative emission from CO_2, TW Hya, this OH line is contaminated by ~20% of the measured line flux. For the 30,000 K OH lines, we select four, and we sum their

Table 3
Linear Regression Parameters for Correlations with LogL_{acc} as Measured in the Reference JDISCS-C1 Sample Excluding Disks with Cavities

Line ID	E_u (K)	λ (μm)	a (σ) -	b (σ) -	PCC logL_{acc}	PCC -log$L_\star$	PCC -n_{13-26}
CO $v = 1$–0	4862, 5004	4.92, 4.93	0.594 (0.066)	−4.235 (0.095)	0.91	0.52	−0.43
CO $v = 2$–1	7501, 8031	4.95, 4.99	0.554 (0.053)	−4.582 (0.060)	0.92	0.60	−0.55
H_2O $v = 1$–1	6006	17.19	0.468 (0.069)	−5.718 (0.078)	0.88	0.45	−0.42
H_2O 6000 K	6052	17.32	0.523 (0.072)	−5.087 (0.097)	0.88	0.59	−0.32
H_2O 3600 K	3646	17.50	0.533 (0.078)	−4.787 (0.114)	0.86	0.54	−0.37
H_2O 2400 K	2433	17.36	0.488 (0.091)	−4.706 (0.132)	0.79	0.56	−0.31
H_2O 1500 K	1448, 1615	23.82, 23.90	0.446 (0.091)	−4.436 (0.132)	0.77	0.53	−0.28
OH 30,000 K	26,716–35,575	9.48–10.23	0.333 (0.074)	−5.323 (0.095)	0.81	0.74	−0.52
OH 10,000 K	10,754	14.62	0.436 (0.079)	−5.486 (0.115)	0.80	0.48	−0.38
OH 6000 K	5495, 7072	17.73, 20.00	0.474 (0.061)	−5.287 (0.084)	0.89	0.58	−0.37
OH 4000 K	3473, 4104	23.07, 25.09	0.418 (0.052)	−5.136 (0.075)	0.89	0.56	−0.46
OH 900 K	875	24.64	0.203 (0.082)	−5.741 (0.107)	0.58	0.32	−0.01
HCN	2000–3700	13.963–13.984	0.395 (0.108)	−4.945 (0.160)	0.68	0.61	−0.28
C_2H_2	1800–3500	13.658–13.677	0.284 (0.111)	−5.086 (0.172)	0.58	0.61	−0.47
CO_2	1000–2800	14.959–14.987	0.302 (0.119)	−4.813 (0.177)	0.54	0.38	−0.01

Note. Linear relations are in the form $\log(L_{line}/L_\odot) = a \times \log(L_{acc}/L_\odot) + b$. The second and third columns indicate the value in upper level energy and wavelength included in each tracer, or their range if multiple lines are included (see Appendix C). In the case of organics, the observed emission features are blends of 10–30 lines even over the small ranges considered here. The PCC value is the Pearson linear correlation coefficient; the second to last column reports the PCC with log$L_\star$, showing that it is systematically lower than that measured with logL_{acc} except for the case of C_2H_2.

Table 4
Line Flux Measurements from MIRI Spectra of Disk Cavities Included in This Work

Target	H_2O 6000 K	H_2O 3600 K	H_2O 2400 K	H_2O 1500 K	H_2O 1448 K	H_2O $v = 1$–1	CO $v = 1$–0	CO $v = 2$–1
GMAur	0.13(0.02)	0.46(0.05)	0.79(0.04)	3.92(0.76)	2.33(0.42)	0.04(0.04)	2.75(0.47)	−0.36(0.23)
HD143006	0.21(0.26)	−0.03(0.29)	0.28(0.23)	−0.98(1.94)	−1.11(0.99)	0.15(0.20)	2.95(0.69)	−0.80(1.51)
HPTau	2.21(0.23)	3.96(0.15)	4.41(0.35)	12.86(1.03)	6.97(0.65)	0.14(0.18)	12.01(1.28)	1.59(0.58)
IPTau	1.15(0.09)	2.36(0.04)	2.91(0.10)	6.11(0.55)	3.47(0.32)	0.07(0.03)	5.74(0.49)	0.38(0.30)
PDS70	0.11(0.05)	0.20(0.06)	0.40(0.09)	1.06(0.09)	0.58(0.04)	0.01(0.04)	0.30(0.92)	−0.60(0.74)
RYLup	0.36(0.27)	1.19(0.40)	1.67(0.12)	7.17(1.15)	3.62(0.53)	0.17(0.18)	15.26(1.12)	1.30(3.17)
SR4	4.98(0.29)	6.25(0.25)	5.66(0.32)	8.88(1.98)	4.57(0.79)	0.84(0.15)	27.73(1.47)	6.19(0.72)
SYCha	0.58(0.15)	1.65(0.08)	2.92(0.07)	9.39(0.37)	5.45(0.22)	0.22(0.14)	2.17(0.29)	0.67(0.69)
Sz129	1.44(0.04)	2.64(0.04)	3.52(0.04)	9.72(0.26)	5.38(0.11)	0.30(0.13)	7.15(0.45)	0.99(0.22)
TCha	0.76(0.36)	0.54(0.26)	−0.28(0.30)	−0.97(2.36)	−1.71(1.18)	0.33(0.15)	−0.21(1.93)	−0.34(1.29)
TWCha	3.43(0.17)	6.27(0.16)	8.64(0.17)	19.45(0.48)	10.41(0.30)	0.56(0.06)	14.25(1.07)	3.93(0.44)
TWHya	0.69(0.15)	1.42(0.28)	5.71(0.35)	29.87(1.71)	16.06(0.82)	0.25(0.26)	4.91(2.02)	−2.95(1.32)

Target	OH 30,000 K	OH 10,000 K	OH 6000 K	OH 4000 K	OH 900 K	HCN	C_2H_2	CO_2
GMAur	3.44(0.31)	0.16(0.04)	0.94(0.34)	3.12(0.19)	1.68(0.10)	0.05(0.05)	0.05(0.04)	−0.69(0.14)
HD143006	−1.17(1.74)	−0.04(0.13)	0.14(0.49)	0.07(0.83)	−0.07(1.37)	−0.21(0.15)	−0.15(0.14)	0.58(1.42)
HPTau	3.63(0.81)	1.15(0.11)	2.95(0.77)	5.40(0.36)	1.21(0.20)	1.62(0.25)	0.73(0.22)	11.01(0.45)
IPTau	1.26(0.34)	0.31(0.08)	0.98(0.06)	1.93(0.32)	0.53(0.36)	1.14(0.06)	0.27(0.06)	1.03(0.15)
PDS70	−1.01(1.04)	0.07(0.02)	0.07(0.05)	0.50(0.13)	0.10(0.03)	0.05(0.05)	0.11(0.07)	0.55(0.47)
RYLup	2.13(2.57)	−0.10(0.14)	1.28(0.42)	3.71(0.29)	1.72(0.45)	0.00(0.23)	0.09(0.32)	0.65(0.78)
SR4	4.88(1.25)	1.48(0.21)	4.96(0.96)	5.68(0.33)	1.87(0.56)	4.31(0.28)	5.93(0.35)	5.17(0.49)
SYCha	1.22(0.84)	0.45(0.08)	0.76(0.13)	1.66(0.22)	0.96(0.03)	0.79(0.27)	0.38(0.21)	2.66(0.38)
Sz129	2.66(0.32)	0.60(0.04)	1.76(0.20)	3.60(0.20)	1.25(0.04)	0.14(0.03)	0.01(0.06)	0.33(0.11)
TCha	1.08(1.00)	−0.10(0.10)	0.58(0.90)	0.82(1.00)	−0.81(1.11)	0.63(0.22)	−0.22(0.15)	−0.28(0.88)
TWCha	3.01(0.49)	0.98(0.11)	2.36(0.09)	4.05(0.16)	1.23(0.14)	4.42(0.07)	1.58(0.07)	0.76(0.15)
TWHya	9.25(1.03)	0.74(0.21)	1.49(0.15)	8.38(1.19)	5.84(0.33)	−0.19(0.39)	−0.29(0.56)	8.65(1.34)

Note. Lines are labeled as defined in Table 3 and Section 3. Line fluxes and errors are reported in units of 10^{-15} erg s^{-1} cm^{-2}. 1σ errors are shown in parentheses. Negative flux values in nondetections are typically due to fringe residuals (see, e.g., Figure 14).

flux to increase S/N due to their typical weakness. For the broad organic emission features, we select smaller ranges with minimal contamination from other molecules. We remark that, to correctly consider contamination from water, the HITRAN line list must be complemented with the HITEMP line list (L. S. Rothman et al. 2010), which includes several high-energy lines that significantly contaminate organic emission (A. Banzatti et al. 2025). In the case of C_2H_2, the only range that can be used is around 13.66 μm, with mild contamination from HCN. The peak of C_2H_2 emission at 13.71–13.72 μm is instead contaminated by multiple water and HCN transitions (Figure 16). In the case of HCN, there are two viable options

Table 5
Line Flux Measurements from MIRI Spectra of Full Disks Included in This Work

Target	H_2O 6000 K	H_2O 3600 K	H_2O 2400 K	H_2O 1500 K	H_2O 1448 K	H_2O $v = 1$–1	CO $v = 1$–0	CO $v = 2$–1
AS205N	30.55(2.04)	70.07(2.71)	99.27(2.66)	162.87(10.62)	88.58(5.11)	9.99(1.49)	169.35(12.88)	97.99(12.36)
AS209	3.55(0.27)	6.03(0.56)	4.69(1.33)	16.53(3.54)	9.28(1.76)	1.08(1.11)	32.62(3.07)	7.00(3.29)
CITau	5.36(0.30)	7.15(0.13)	7.31(0.21)	11.91(0.34)	5.70(0.23)	1.09(0.02)	29.52(1.92)	12.84(0.88)
DoAr25	1.21(0.09)	2.52(0.13)	2.80(0.12)	4.71(0.53)	2.27(0.34)	0.21(0.03)	7.28(0.98)	−0.11(0.57)
DoAr33	0.75(0.05)	1.70(0.05)	2.12(0.11)	3.34(0.18)	1.62(0.11)	0.07(0.03)	2.42(0.49)	−0.27(0.36)
Elias20	6.91(0.24)	16.93(0.44)	25.23(0.54)	54.15(0.87)	27.91(0.52)	1.93(0.37)	65.96(4.50)	25.79(2.60)
Elias24	14.43(0.47)	36.30(0.93)	58.43(0.76)	123.84(1.01)	64.49(0.06)	2.68(0.29)	95.99(6.63)	33.02(5.56)
Elias27	5.70(0.20)	11.78(0.21)	14.38(0.37)	25.93(0.61)	13.46(0.17)	1.13(0.13)	47.21(3.52)	20.33(2.59)
FZTau	15.34(1.00)	29.10(1.30)	35.43(0.61)	51.04(0.82)	24.99(0.24)	4.04(0.20)	104.67(11.29)	58.17(7.74)
GKTau	3.61(0.34)	7.01(0.31)	10.08(0.25)	26.22(0.73)	14.37(0.47)	0.64(0.13)	27.08(1.49)	8.00(0.78)
GOTau	0.16(0.02)	0.46(0.02)	0.52(0.02)	1.12(0.15)	0.59(0.07)	0.01(0.01)	1.51(0.14)	−0.13(0.14)
GQLup	2.87(0.18)	7.54(0.26)	12.83(0.10)	34.46(0.43)	18.27(0.25)	0.67(0.16)	47.05(1.58)	9.60(1.73)
IQTau	3.32(0.16)	4.11(0.17)	4.91(0.19)	11.36(0.41)	6.30(0.23)	0.95(0.02)	7.95(1.65)	8.35(1.52)
IRAS-04385	1.36(0.11)	4.50(0.22)	9.54(0.28)	26.39(1.17)	15.06(0.80)	0.40(0.15)	3.91(0.30)	1.13(0.36)
MYLup	0.03(0.07)	0.23(0.03)	0.61(0.03)	1.64(0.34)	0.81(0.17)	−0.09(0.06)	1.06(0.32)	−0.66(0.27)
RULup	15.35(1.02)	26.28(1.24)	31.23(0.60)	44.25(2.46)	22.40(1.35)	3.40(0.55)	103.17(8.97)	42.74(6.27)
Sz114	1.24(0.06)	3.14(0.03)	4.49(0.04)	11.64(0.50)	6.44(0.17)	0.37(0.08)	10.28(0.44)	2.88(1.04)
VZCha	5.01(0.24)	7.18(0.28)	7.90(0.24)	18.20(0.12)	9.47(0.08)	0.89(0.05)	46.48(3.98)	15.50(2.04)
WSB52	12.07(0.40)	30.49(0.48)	43.45(0.42)	67.68(1.56)	34.85(0.88)	2.02(0.10)	29.54(1.29)	10.59(0.59)
n_{13-26}	OH 30,000 K	OH 10,000 K	OH 6000 K	OH 4000 K	OH 900 K	HCN	C_2H_2	CO_2
0.03	3.14(17.63)	13.17(2.10)	18.49(1.99)	21.95(4.18)	6.86(1.47)	60.38(4.29)	40.47(4.23)	155.34(6.75)
−0.04	−10.66(9.50)	3.74(0.28)	3.94(1.93)	7.42(1.85)	6.57(1.98)	1.84(3.39)	1.24(2.94)	6.64(5.22)
−0.18	3.79(0.62)	2.00(0.09)	3.41(0.13)	4.55(0.15)	0.53(0.61)	9.44(0.19)	8.85(0.16)	7.04(0.35)
0.43	1.14(0.30)	0.16(0.05)	0.44(0.09)	1.52(0.07)	0.25(0.21)	8.60(0.09)	2.07(0.10)	5.18(0.19)
−0.87	−0.09(0.52)	0.44(0.06)	0.50(0.07)	1.37(0.12)	0.11(0.16)	4.49(0.10)	5.02(0.10)	4.50(0.24)
−0.69	4.77(0.69)	3.90(0.75)	5.85(0.26)	8.65(0.30)	0.98(0.33)	24.71(0.43)	32.26(0.40)	18.75(0.53)
−0.63	3.99(3.51)	7.45(1.08)	7.62(1.21)	11.85(0.33)	4.62(2.07)	50.60(1.81)	50.62(1.97)	54.00(1.46)
−0.46	2.64(0.52)	2.39(0.11)	3.39(0.15)	5.10(0.16)	2.34(0.71)	2.17(0.14)	0.30(0.21)	10.24(0.54)
−0.81	13.33(3.02)	6.29(0.57)	7.07(0.49)	10.08(0.74)	2.14(0.32)	13.99(0.37)	5.13(0.37)	41.61(0.91)
−0.09	5.38(1.20)	2.24(0.23)	4.18(0.18)	7.59(0.44)	3.14(0.61)	0.60(0.18)	0.17(0.19)	3.23(0.42)
0.16	0.52(0.13)	0.10(0.03)	0.30(0.08)	0.69(0.06)	0.10(0.04)	0.60(0.03)	2.02(0.03)	0.93(0.06)
−0.19	5.07(0.94)	1.61(0.07)	4.38(0.08)	9.20(0.35)	1.40(0.41)	3.86(0.20)	0.01(0.27)	4.53(0.42)
−0.4	3.46(0.61)	1.33(0.25)	2.97(0.13)	3.58(0.24)	1.48(0.24)	6.10(0.20)	2.39(0.13)	2.16(0.31)
0.73	1.70(0.52)	0.75(0.11)	0.88(0.27)	1.27(0.27)	1.12(0.53)	4.17(0.15)	3.19(0.15)	14.56(0.29)
0.4	0.07(0.34)	0.50(0.10)	0.07(0.13)	0.31(0.15)	0.36(0.15)	1.36(0.11)	0.61(0.14)	8.89(0.33)
0.07	4.68(2.90)	4.86(0.82)	7.20(1.68)	11.98(0.76)	2.91(0.06)	16.68(0.79)	2.25(0.83)	25.60(1.97)
0.02	1.25(0.24)	1.33(0.22)	0.64(0.11)	1.57(0.14)	1.25(0.09)	2.33(0.08)	3.02(0.11)	18.25(0.17)
−1.02	3.66(0.64)	1.57(0.07)	4.05(0.15)	5.67(0.17)	0.46(0.12)	6.02(0.18)	6.06(0.12)	3.13(0.27)
−0.22	5.36(0.73)	4.66(0.20)	3.06(0.85)	4.62(0.33)	3.89(0.42)	24.10(0.38)	21.54(0.42)	65.32(0.92)

Note. Same as Table 4 but for the JDISCS-C1 sample. The n_{13-26} index is included in the bottom half of the table (which corresponds to the same targets as in the upper half) because the improved absolute flux calibration in JDISCS reduction 9.0 has changed the continuum flux by up to 10%–20% in channel 4 and in turn it has changed all the measured values from those previously measured in reduction 8.0 and published in N. Arulanantham et al. (2025).

that cover HCN emission dominated by slightly different upper energy levels; we tested correlations with both and decided to use the 13.97 μm because it better matches the energy range covered in C_2H_2 too (Table 3).

CO_2 is the only case where avoiding contamination is impossible, because multiple species overlap with it including a strong H_2O line (which can be relatively easily removed), HCN, OH, and even H I (the 16–10 line). In this work, we decide to correct the measured CO_2 line flux from HI contamination, by measuring and removing the line flux from the next HI line in the series (the 15–10 line at 16.41 μm), and from H_2O contamination by subtracting twice the flux measured in an uncontaminated line at 11.27 μm with same upper level energy (∼8200 K) and lower Einstein-A coefficient (A_{ul}) of ∼17 s^{-1} as the one contaminating CO_2 (which has ∼8200 K and A_{ul} of ∼62 s^{-1}). The factor of 2 in line flux is applied to account for the different A_{ul}, as determined in the case of TW Cha where there is no CO_2 emission. A little residual contamination from OH may still remain in CO_2, but we do not attempt to correct for that due to the complex excitation of OH (Section 3.3). We remark that a slab model to the CO_2 emission would not necessarily give a more reliable estimate of the uncontaminated line flux, especially because slab model fits typically ignore the contamination from OH and H I and may not reproduce well the high-energy H_2O line either.

Appendix D
Additional Comparisons to Previous Work

D.1. Comparison to Previous Classifications

We compare the MR/MP dichotomy introduced in this work to previous classifications of cavity disks. One of the dust cavity classifications that has taken more ground in the

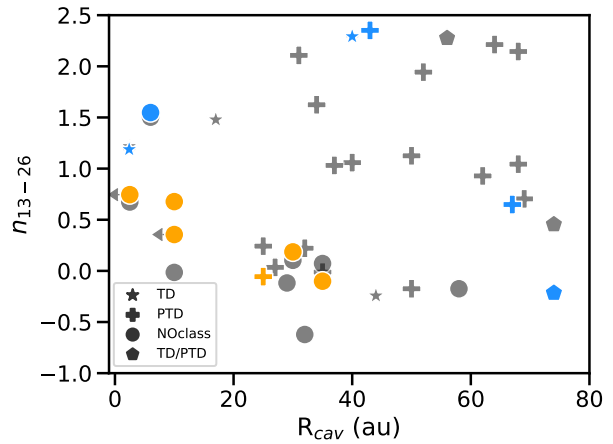

Figure 17. IR index n_{13-26} against millimeter-cavity radius $R_{\rm cav}$, with TD and PTD classifications adopted from C. Espaillat et al. (2014) and L. Francis & N. van der Marel (2020), which in a few cases do not agree (marked as TD/PTD in this figure). Some disks do not have a previous classification in these papers (marked as NOclass), including most of the MR cavities. The gray data points show millimeter cavities from P. Pinilla et al. (2018b) and L. Francis & N. van der Marel (2020) matched to the IR index measured from Spitzer spectra (Appendix B). The molecular dichotomy presented in this work is included with same colors as in Figure 8, with n_{13-26} from MIRI (Table 1).

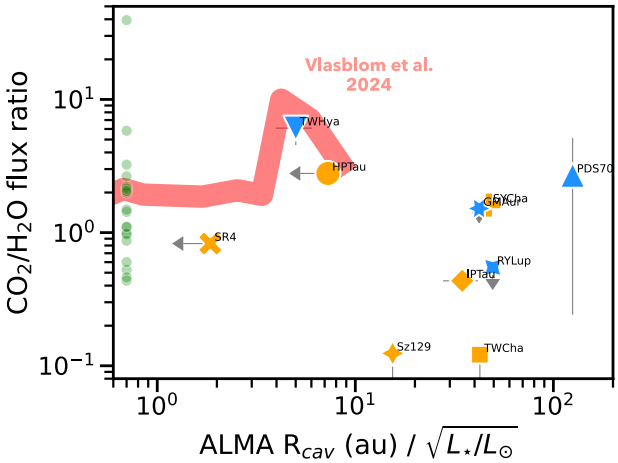

Figure 18. Ratio between CO_2 and H_2O line fluxes as a function of cavity size, compared to predictions from M. Vlasblom et al. (2024). The water line used in this figure is the 3600 K line at 17.50 μm selected in A. Banzatti et al. (2025) and reported in Table 3. The green points show the reference JDISCS-C1 sample of full disks as in previous figures, placed at an x-axis value of 0.7 just for illustration.

literature is that into "TD" and "PTD" disks, based on an IR excess interpreted as indicating residual inner dust belts within a larger dust cavity in the latter (C. Espaillat et al. 2007, 2014). This classification was based on spatially unresolved SED modeling and has later been put into question due to limitations and degeneracies of using the NIR excess to detect an inner dust belt (T. Kaeufer et al. 2023; N. van der Marel 2023). By comparison to previous work, we can conclude that the TD/PTD classification does not simply map into the MR/MP dichotomy, as shown in Figure 17: PTD disks cover most of the parameter space in n_{13-26} and $R_{\rm cav}$ without distinctions in either parameter, while the MR/MP dichotomy shows very specific segregation in this plot (Figure 8). One possibility is that the separation into MR and MP is larger in n_{13-26} than in the IR excess at shorter wavelengths.

Additional classifications have been proposed based on other observables. C. Salyk et al. (2009) proposed the existence of two disk classes based on CO detections and accretion rates: "cleared" inner disks and "partially depleted" inner disks (with stronger CO emission and higher accretion rate). This classification too is different from the dichotomy introduced in this work, because MR and MP span the same range in accretion luminosity. Another classification was proposed by J. E. Owen & C. J. Clarke (2012) and J. E. Owen (2016) based on millimeter luminosity and accretion rate, with "millimeter-faint" and low-accreting disks being consistent with disk dispersal through photoevaporation while "millimeter-bright" disks are challenging to explain both with photoevaporative winds and planets. Again, this classification is not connected to the MR/MP dichotomy, which are not separated by accretion rates. We should also note that disks around intermediate-mass stars and Herbig Ae/Be stars, the latter being excluded from this work, have often affected and possibly biased all these previous classifications. Large dust cavities are found to be more frequent in disks around stars $>1.5\,M_\odot$ (N. van der Marel 2023); they appear to have high accretion rates and might have more extreme conditions than disk cavities around solar-mass stars (J. E. Owen & C. J. Clarke 2012; B. Ercolano & I. Pascucci 2017).

D.2. On CO_2 Emission as a Tracer of Inner Disk Cavities

Recent modeling work by M. Vlasblom et al. (2024) proposed that the CO_2 Q-branch emission relative to water emission observed with MIRI may be a tracer of small inner disk cavities, with larger CO_2/H_2O ratios when the cavity size is in between the H_2O and CO_2 snowlines (between 0.5 and 2 au in their fiducial model). We test this idea in Figure 18, where the CO_2/H_2O ratio measured in this sample is compared to model predictions from Figure B.7 in M. Vlasblom et al. (2024) as normalized to the square root of the stellar luminosity. In this work, we use the 3600 K water line at 17.50 μm selected in A. Banzatti et al. (2025), which is sensitive to the warm water reservoir; the model track shown in the figure is also updated to this line. The models show a peak in the CO_2/H_2O flux ratio at values of $\sim$4 au / $\sqrt{L_\star/L_\odot}$, decreasing at larger radii when the cavity size reaches and surpasses the CO_2 snowline.

In this work, we only have three disks that overlap with model predictions from M. Vlasblom et al. (2024): TW Hya, HP Tau, and SR 4; the latter two, however, have an uncertain inner disk cavity (positive IR index but undetected millimeter cavity). The model peak in the CO_2/H_2O ratio overlaps with TW Hya, while the rest of the sample sits at values >10 au/ $\sqrt{L_\star/L_\odot}$ and shows a large range of ratios (as small as <0.1 and as large as 2). On the other hand, the reference sample of full disks also span a similar range of CO_2/H_2O ratios (green points in the figure), showing that either small dust cavities are very common or this ratio might be sensitive to other processes than just an inner dust cavity. It is clear that more disks with small cavities are needed to test the models and any dependence of the CO_2/H_2O ratio on cavity size. Moreover, if the millimeter-cavity size does not trace the innermost cavity size in smaller dust, the comparison to the models (which assume a completely devoid inner cavity for simplicity) needs to be updated with more sophisticated models that account for a different distribution of sub-μm dust and larger solid grains.

D.3. The Peculiar Case of PDS 70

The water emission observed in PDS 70 stands out as an outlier in the sample of disk cavities under multiple aspects, as shown above in Figures 4 and 5. Its spectrum is consistent with a single, warm ($T \sim 400$ K), optically thick ($\sim 5 \times 10^{18}$ cm^{-2}) inner water reservoir emitting from $\sim$0.1 au (assuming the resolved line broadening is from Keplerian rotation around the star) unlike any other MP cavity, where emission is more optically thin and comes from larger radii. It is the only disk so far where a single slab model to the emission of rotational lines at 10–27 μm does not overpredict the rovibrational water band at 6–8 μm (G. Perotti et al. 2023), again pointing to a small and highly dense emitting region. The emitting area is small and of the order of $\sim$0.007 au^2. The origin of this unusual emission could be an inner dust belt where water survives, which may be detected in millimeter emission with ALMA (L. Francis & N. van der Marel 2020; M. Benisty et al. 2021) and could still be fed by some residual filtration of ice carried inward on small dust grains even through the very large cavity (H. Jang et al. 2024; P. Pinilla et al. 2024). An alternative, interesting scenario that might offer an explanation for the peculiar water emission observed in this disk is that it could instead be from a circumplanetary disk around one of the protoplanets detected in this system (M. Benisty et al. 2021). The circumplanetary disk is not spatially resolved with ALMA, but the emitting area of water emission is small enough to be consistent with it.

The MIRI spectrum also offers a tentative detection of HCN and C_2H_2 too, which seem to be colder than in other disks (G. Perotti et al. 2025, in preparation). The IR index has been observed to be highly variable between -0.22 in the MIRI spectrum and 0.5 in a previous Spitzer spectrum in 2007 (G. Perotti et al. 2023), showing highly variable inner disk dust content or geometry (E. Gaidos et al. 2024; H. Jang et al. 2024). This system should be monitored with MIRI to determine if the molecular spectrum is variable too. The SED variability in PDS 70, recently observed in another MP cavity T Cha (C. Xie et al. 2025), also poses the question of whether it could be common in MP cavities in general, something that should be tested in future work.

ORCID iDs

Patrick Mallaney https://orcid.org/0009-0005-2400-6946
Andrea Banzatti https://orcid.org/0000-0003-4335-0900
Colette Salyk https://orcid.org/0000-0003-3682-6632
Ilaria Pascucci https://orcid.org/0000-0001-7962-1683
Paola Pinilla https://orcid.org/0000-0001-8764-1780
Joan Najita https://orcid.org/0000-0002-5758-150X
Klaus M. Pontoppidan https://orcid.org/0000-0001-7552-1562
Sebastiaan Krijt https://orcid.org/0000-0002-3291-6887
Geoffrey A. Blake https://orcid.org/0000-0003-0787-1610
Benoît Tabone https://orcid.org/0000-0002-1103-3225
Till Kaeufer https://orcid.org/0000-0001-8240-978X
Ke Zhang https://orcid.org/0000-0002-0661-7517
Feng Long https://orcid.org/0000-0002-7607-719X
Jane Huang https://orcid.org/0000-0001-6947-6072
Giovanni Rosotti https://orcid.org/0000-0003-4853-5736
Karin I. Öberg https://orcid.org/0000-0001-8798-1347
María José Colmenares https://orcid.org/0000-0002-5296-6232
Lucas A. Cieza https://orcid.org/0000-0002-2828-1153
L. Ilsedore Cleeves https://orcid.org/0000-0003-2076-8001
Joe Williams https://orcid.org/0009-0008-8176-1974
Chengyan Xie https://orcid.org/0000-0001-8184-5547
Miguel Vioque https://orcid.org/0000-0002-4147-3846
Mayank Narang https://orcid.org/0000-0002-0554-1151
Nicholas P. Ballering https://orcid.org/0000-0002-4276-3730
Minjae Kim https://orcid.org/0000-0001-6218-2004

References

Alcala, J. M., Krautter, J., Covino, E., et al. 1997, A&A, 319, 184
Alexander, R., Pascucci, I., Andrews, S., Armitage, P., & Cieza, L. 2014, in Protostars and Planets VI, ed. H. Beuther et al. (Univ. Arizona Press), 475
Anderson, D. E., Blake, G. A., Cleeves, L. I., et al. 2021, ApJ, 909, 55
Andrews, S. M., Huang, J., Pérez, L. M., et al. 2018a, ApJL, 869, L41
Andrews, S. M., Terrell, M., Tripathi, A., et al. 2018b, ApJL, 865, 157
Andrews, S. M., Wilner, D. J., Espaillat, C., et al. 2011, ApJ, 732, 42
Andrews, S. M., Wilner, D. J., Zhu, Z., et al. 2016, ApJL, 820, L40
Ansdell, M., Williams, J. P., van der Marel, N., et al. 2016, ApJ, 828, 46
Arabhavi, A. M., Kamp, I., Henning, T., et al. 2025, A&A, 699, A194
Arulanantham, N., Salyk, C., Pontoppidan, K., et al. 2025, AJ, 170, 67
Astropy Collaboration, Price-Whelan, A. M., Lim, P. L., et al. 2022, ApJ, 935, 167
Astropy Collaboration, Price-Whelan, A. M., Sipőcz, B. M., et al. 2018, AJ, 156, 123
Astropy Collaboration, Robitaille, T. P., Tollerud, E. J., et al. 2013, A&A, 558, A33
Bajaj, N. S., Pascucci, I., Gorti, U., et al. 2024, AJ, 167, 127
Ballering, N. P., & Eisner, J. A. 2019, AJ, 157, 144
Banzatti, A., Abernathy, K. M., Brittain, S., et al. 2022, AJ, 163, 174
Banzatti, A., Garufi, A., Kama, M., et al. 2018, A&A, 609, L2
Banzatti, A., Meyer, M. R., Bruderer, S., et al. 2012, ApJ, 745, 90
Banzatti, A., Pascucci, I., Bosman, A. D., et al. 2020, ApJ, 903, 124
Banzatti, A., & Pontoppidan, K. M. 2015, ApJ, 809, 167
Banzatti, A., Pontoppidan, K. M., Bruderer, S., Muzerolle, J., & Meyer, M. R. 2015, ApJL, 798, L16
Banzatti, A., Pontoppidan, K. M., Carr, J. S., et al. 2023, ApJL, 957, L22
Banzatti, A., Pontoppidan, K. M., Salyk, C., et al. 2017, ApJ, 834, 152
Banzatti, A., Salyk, C., Pontoppidan, K. M., et al. 2025, AJ, 169, 165
Baraffe, I., Homeier, D., Allard, F., & Chabrier, G. 2015, A&A, 577, A42
Benisty, M., Bae, J., Facchini, S., et al. 2021, ApJL, 916, L2
Bethell, T., & Bergin, E. 2009, Sci, 326, 1675
Birnstiel, T. 2024, ARA&A, 62, 157
Bosman, A. D., Banzatti, A., Bruderer, S., et al. 2019, A&A, 631, A133
Bosman, A. D., Bergin, E. A., Calahan, J., & Duval, S. E. 2022, ApJL, 930, L26
Bouvier, J., Perraut, K., Le Bouquin, J. B., et al. 2020, A&A, 636, A108
Brown, J. M., Blake, G. A., Dullemond, C. P., et al. 2007, ApJL, 664, L107
Brown, J. M., Blake, G. A., Qi, C., et al. 2009, ApJ, 704, 496
Brown, J. M., Pontoppidan, K. M., van Dishoeck, E. F., et al. 2013, ApJ, 770, 94
Bruderer, S. 2013, A&A, 559, A46
Bushouse, H., Eisenhamer, J., Dencheva, N., et al. 2024, JWST Calibration Pipeline, v1.15.1,, Zenodo, doi:10.5281/zenodo.12692459
Calvet, N., D'Alessio, P., Hartmann, L., et al. 2002, ApJ, 568, 1008
Calvet, N., Muzerolle, J., Briceño, C., et al. 2004, AJ, 128, 1294
Carr, J. S., & Najita, J. R. 2014, ApJ, 788, 66
Cieza, L. A., González-Ruilova, C., Hales, A. S., et al. 2021, MNRAS, 501, 2934
Claes, R. A. B., Manara, C. F., Garcia-Lopez, R., et al. 2022, A&A, 664, L7
Colmenares, M. J., Bergin, E. A., Salyk, C., et al. 2024, ApJ, 977, 173
Currie, T., & Sicilia-Aguilar, A. 2011, ApJ, 732, 24
D'Alessio, P., Calvet, N., Hartmann, L., Franco-Hernández, R., & Servín, H. 2006, ApJ, 638, 314
D'Alessio, P., Hartmann, L., Calvet, N., et al. 2005, ApJ, 621, 461
Deng, D., Pascucci, I., & Fernandes, R. B. 2025, JOSS, 10, 7493
Dodson-Robinson, S. E., & Salyk, C. 2011, ApJ, 738, 131
Doppmann, G. W., Najita, J. R., & Carr, J. S. 2017, ApJ, 836, 242
Dutrey, A., Guilloteau, S., Piétu, V., et al. 2008, A&A, 490, L15
Duval, S. E., Bosman, A. D., & Bergin, E. A. 2022, ApJL, 934, L25
Ercolano, B., & Pascucci, I. 2017, RSOS, 4, 170114
Espaillat, C., Calvet, N., D'Alessio, P., et al. 2007, ApJL, 670, L135
Espaillat, C., D'Alessio, P., Hernández, J., et al. 2010, ApJ, 717, 441
Espaillat, C., Furlan, E., D'Alessio, P., et al. 2011, ApJ, 728, 49

Espaillat, C., Muzerolle, J., Najita, J., et al. 2014, in Protostars and Planets VI, ed. H. Beuther et al. (Univ. Arizona Press), 497
Espaillat, C. C., Thanathibodee, T., Pittman, C. V., et al. 2023, ApJL, 958, L4
Espaillat, C. C., Thanathibodee, T., Zhu, Z., et al. 2024, ApJL, 973, L16
Fang, M., Pascucci, I., Edwards, S., et al. 2018, ApJ, 868, 28
Fasano, D., Benisty, M., Curone, P., et al. 2025, A&A, 699, A373
Fedele, D., Bruderer, S., van Dishoeck, E. F., et al. 2013, A&A, 559, A77
Feiden, G. A. 2016, A&A, 593, A99
Fiorellino, E., Alcalá, J. M., Manara, C. F., et al. 2025, A&A, 704, A42
Francis, L., & van der Marel, N. 2020, ApJ, 892, 111
Furlan, E., Hartmann, L., Calvet, N., et al. 2006, ApJS, 165, 568
Furlan, E., Luhman, K. L., Espaillat, C., et al. 2011, ApJS, 195, 3
Furlan, E., Watson, D. M., McClure, M. K., et al. 2009, ApJ, 703, 1964
Gaia Collaboration, Prusti, T., de Bruijne, J. H. J., et al. 2016, A&A, 595, A1
Gaia Collaboration, Vallenari, A., Brown, A. G. A., et al. 2023, A&A, 674, A1
Gaidos, E., Thanathibodee, T., Hoffman, A., et al. 2024, ApJ, 966, 167
Gárate, M., Delage, T. N., Stadler, J., et al. 2021, A&A, 655, A18
Garufi, A., Quanz, S. P., Avenhaus, H., et al. 2013, A&A, 560, A105
Gasman, D., Temmink, M., van Dishoeck, E. F., et al. 2025, A&A, 694, A147
Glassgold, A. E., Meijerink, R., & Najita, J. R. 2009, ApJ, 701, 142
Gordon, I. E., Rothman, L. S., Hargreaves, R. J., et al. 2022, JQSRT, 277, 107949
Grant, S. L., Temmink, M., van Dishoeck, E. F., et al. 2025, A&A, 702, A126
Greenwood, A. J., Kamp, I., Waters, L. B. F. M., Woitke, P., & Thi, W. F. 2019, A&A, 626, A6
Haffert, S. Y., Bohn, A. J., de Boer, J., et al. 2019, NatAs, 3, 749
Hendler, N. P., Pinilla, P., Pascucci, I., et al. 2018, MNRAS, 475, L62
Henning, T., Kamp, I., Samland, M., et al. 2024, PASP, 136, 054302
Herczeg, G. J., & Hillenbrand, L. A. 2014, ApJ, 786, 97
Hernández, J., Hartmann, L., Megeath, T., et al. 2007, ApJ, 662, 1067
Hoadley, K., France, K., Alexander, R. D., McJunkin, M., & Schneider, P. C. 2015, ApJ, 812, 41
Huang, J., Andrews, S. M., Dullemond, C. P., et al. 2018, ApJL, 869, L42
Huang, J., Andrews, S. M., Dullemond, C. P., et al. 2020, ApJ, 891, 48
Huang, S., van der Marel, N., & Portegies Zwart, S. 2024, A&A, 691, A155
Hughes, A. M., Wilner, D. J., Calvet, N., et al. 2007, ApJ, 664, 536
Hunter, J. D. 2007, CSE, 9, 90
Ingleby, L., Calvet, N., Bergin, E., et al. 2011, ApJ, 743, 105
Jang, H., Waters, R., Kaeufer, T., et al. 2024, A&A, 691, A148
Jellison, E. G., Banzatti, A., Johnson, M. B., & Bruderer, S. 2024, AJ, 168, 99
Johnson, M., Banzatti, A., Fuller, J., & Jellison, E. 2024, spexod/iSLAT: Second release, vv4.03,, Zenodo, doi:10.5281/zenodo.12167853
Kaeufer, T., Woitke, P., Min, M., Kamp, I., & Pinte, C. 2023, A&A, 672, A30
Kaeufl, H.-U., Ballester, P., Biereichel, P., et al. 2004, SPIE, 5492, 1218
Kamp, I., Henning, T., Arabhavi, A. M., et al. 2023, FaDi, 245, 112
Kamp, I., Thi, W.-F., Woitke, P., et al. 2017, A&A, 607, A41
Kanwar, J., Kamp, I., Jang, H., et al. 2024, A&A, 689, A231
Kanwar, J., Kamp, I., Woitke, P., et al. 2026, A&A, 705, A222
Keppler, M., Benisty, M., Müller, A., et al. 2018, A&A, 617, A44
Koerner, D. W., Sargent, A. I., & Beckwith, S. V. W. 1993, Icar, 106, 2
Krijt, S., Banzatti, A., Zhang, K., et al. 2025, ApJL, 990, L72
Lada, C. J., Muench, A. A., Luhman, K. L., et al. 2006, AJ, 131, 1574
Lommen, D., Wright, C. M., Maddison, S. T., et al. 2007, A&A, 462, 211
Long, F., Herczeg, G. J., Harsono, D., et al. 2019, ApJ, 882, 49
Long, F., Pascucci, I., Houge, A., et al. 2025, ApJL, 978, L30
Loomis, R. A., Öberg, K. I., Andrews, S. M., & MacGregor, M. A. 2017, ApJ, 840, 23
Luhman, K. L., Allen, P. R., Espaillat, C., Hartmann, L., & Calvet, N. 2010, ApJS, 186, 111
Macías, E., Guerra-Alvarado, O., Carrasco-González, C., et al. 2021, A&A, 648, A33
Manara, C. F., Ansdell, M., Rosotti, G. P., et al. 2023, ASPC, 534, 539
Manara, C. F., Testi, L., Natta, A., et al. 2014, A&A, 568, A18
Marsh, K. A., & Mahoney, M. J. 1992, ApJL, 395, L115
Martel, É., & Lesur, G. 2022, A&A, 667, A17
Meijerink, R., Pontoppidan, K. M., Blake, G. A., Poelman, D. R., & Dullemond, C. P. 2009, ApJ, 704, 1471
Merín, B., Brown, J. M., Oliveira, I., et al. 2010, ApJ, 718, 1200
Miotello, A., Kamp, I., Birnstiel, T., Cleeves, L. C., & Kataoka, A. 2023, ASPC, 534, 501
Najita, J. R., Ádámkovics, M., & Glassgold, A. E. 2011, ApJ, 743, 147
Najita, J. R., Carr, J. S., Strom, S. E., et al. 2010, ApJ, 712, 274
Najita, J. R., Strom, S. E., & Muzerolle, J. 2007, MNRAS, 378, 369
Neufeld, D. A., Manoj, P., Tyagi, H., et al. 2024, ApJL, 966, L22
Newville, M., Stensitzki, T., Allen, D. B., & Ingargiola, A. 2014, LMFIT: Non-Linear Least-Square Minimization and Curve-Fitting for Python, v0.8.0,, Zenodo, doi:10.5281/zenodo.11813
Orcajo, S., Cieza, L. A., Guilera, O., et al. 2025, ApJL, 984, L57
Orihara, R., Momose, M., Muto, T., et al. 2023, PASJ, 75, 424
Owen, J. E. 2016, PASA, 33, e005
Owen, J. E., & Clarke, C. J. 2012, MNRAS, 426, L96
Parikka, A., Habart, E., Bernard-Salas, J., et al. 2017, A&A, 599, A20
Pascucci, I., Cabrit, S., Edwards, S., et al. 2023, ASPC, 534, 567
Pascucci, I., Testi, L., Herczeg, G. J., et al. 2016, ApJ, 831, 125
Perotti, G., Christiaens, V., Henning, T., et al. 2023, Natur, 620, 516
Pinilla, P., Benisty, M., Waters, R., Bae, J., & Facchini, S. 2024, A&A, 686, A135
Pinilla, P., Flock, M., Ovelar, M. d. J., & Birnstiel, T. 2016, A&A, 596, A81
Pinilla, P., Natta, A., Manara, C. F., et al. 2018a, A&A, 615, A95
Pinilla, P., Pascucci, I., & Marino, S. 2020, A&A, 635, A105
Pinilla, P., Tazzari, M., Pascucci, I., et al. 2018b, ApJ, 859, 32
Pontoppidan, K. M., Blake, G. A., van Dishoeck, E. F., et al. 2008, ApJ, 684, 1323
Pontoppidan, K. M., Salyk, C., Banzatti, A., et al. 2024, ApJ, 963, 158
Pontoppidan, K. M., Salyk, C., Blake, G. A., & Käufl, H. U. 2010, ApJL, 722, L173
Ramírez-Tannus, M. C., Bik, A., Getman, K. V., et al. 2025, A&A, 701, A139
Rayner, J., Tokunaga, A., Jaffe, D., et al. 2022, PASP, 134, 015002
Rettig, T. W., Haywood, J., Simon, T., Brittain, S. D., & Gibb, E. 2004, ApJL, 616, L163
Rice, W. K. M., Armitage, P. J., Wood, K., & Lodato, G. 2006, MNRAS, 373, 1619
Rieke, G. H., Wright, G. S., Böker, T., et al. 2015, PASP, 127, 584
Romero-Mirza, C. E., Öberg, K. I., Banzatti, A., et al. 2024, ApJ, 964, 36
Romero-Mirza, C. E., Öberg, K. I., Banzatti, A., et al. 2025, ApJ, 991, 128
Rothman, L. S., Gordon, I. E., Barber, R. J., et al. 2010, JQSRT, 111, 2139
Salyk, C., Blake, G. A., Boogert, A. C. A., & Brown, J. M. 2009, ApJ, 699, 330
Salyk, C., Blake, G. A., Boogert, A. C. A., & Brown, J. M. 2011a, ApJ, 743, 112
Salyk, C., Lacy, J., Richter, M., et al. 2019, ApJ, 874, 24
Salyk, C., Lacy, J. H., Richter, M. J., et al. 2015, ApJL, 810, L24
Salyk, C., Pontoppidan, K. M., Banzatti, A., et al. 2025, AJ, 169, 184
Salyk, C., Pontoppidan, K. M., Blake, G. A., Najita, J. R., & Carr, J. S. 2011b, ApJ, 731, 130
Schwarz, K. R., Henning, T., Christiaens, V., et al. 2024, ApJ, 962, 8
Sellek, A. D., Bajaj, N. S., Pascucci, I., et al. 2024, AJ, 167, 223
Shridharan, B., Manoj, P., Pathak, V. C., et al. 2025, arXiv:2512.03456
Sicilia-Aguilar, A., Henning, T., Dullemond, C. P., et al. 2011, ApJ, 742, 39
Skinner, S. L., & Audard, M. 2022, ApJ, 938, 134
Skrutskie, M. F., Dutkevitch, D., Strom, S. E., et al. 1990, AJ, 99, 1187
Smith, S. A., Romero-Mirza, C. E., Banzatti, A., et al. 2025, ApJL, 984, L51
Soderblom, D. R., Hillenbrand, L. A., Jeffries, R. D., Mamajek, E. E., & Naylor, T. 2014, in Protostars and Planets VI, ed. H. Beuther et al. (Univ. Arizona Press), 219
Strom, K. M., Strom, S. E., Edwards, S., Cabrit, S., & Skrutskie, M. F. 1989, AJ, 97, 1451
Tabone, B., Bettoni, G., van Dishoeck, E. F., et al. 2023, NatAs, 7, 805
Tabone, B., van Dishoeck, E. F., & Black, J. H. 2024, A&A, 691, A11
Tabone, B., van Hemert, M. C., van Dishoeck, E. F., & Black, J. H. 2021, A&A, 650, A192
Tappe, A., Lada, C. J., Black, J. H., & Muench, A. A. 2008, ApJL, 680, L117
Temmink, M., Sellek, A. D., Gasman, D., et al. 2025, A&A, 699, A134
Thi, W. F., Kamp, I., Woitke, P., et al. 2013, A&A, 551, A49
Tofflemire, B. M., Manara, C. F., Banzatti, A., et al. 2025, ApJ, 985, 224
van der Marel, N. 2023, EPJP, 138, 225
van der Marel, N., van Dishoeck, E. F., Bruderer, S., Pérez, L., & Isella, A. 2015, A&A, 579, A106
van der Marel, N., Verhaar, B. W., van Terwisga, S., et al. 2016, A&A, 592, A126
van der Marel, N., Williams, J. P., Ansdell, M., et al. 2018, ApJ, 854, 177
van der Marel, N., Williams, J. P., Picogna, G., et al. 2022, arXiv:2204.08225
van der Walt, S., Colbert, S. C., & Varoquaux, G. 2011, CSE, 13, 22
Vioque, M., Booth, R. A., Ragusa, E., et al. 2026, A&A, 705, A238
Virtanen, P., Gommers, R., Oliphant, T. E., et al. 2020, NatMe, 17, 261
Vlasblom, M., Temmink, M., Sellek, A. D., & van Dishoeck, E. F. 2025, A&A, 703, A52
Vlasblom, M., van Dishoeck, E. F., Tabone, B., & Bruderer, S. 2024, A&A, 682, A91
Walsh, C., Nomura, H., & van Dishoeck, E. 2015, A&A, 582, A88
Waskom, M. 2021, JOSS, 6, 3021
Wells, M., Pel, J. W., Glasse, A., et al. 2015, PASP, 127, 646
Wheeler, C. H., Hinkel, N. R., & Banzatti, A. 2024, PASP, 136, 113002
Williams, J. P., & Cieza, L. A. 2011, ARA&A, 49, 67

Woitke, P., Min, M., Pinte, C., et al. 2016, A&A, 586, A103
Woitke, P., Min, M., Thi, W. F., et al. 2018, A&A, 618, A57
Woitke, P., Thi, W. F., Arabhavi, A. M., et al. 2024, A&A, 683, A219
Wright, G. S., Rieke, G. H., Glasse, A., et al. 2023, PASP, 135, 048003
Xie, C., Pascucci, I., Deng, D., et al. 2025, ApJ, 978, 34
Zannese, M., Tabone, B., Habart, E., et al. 2024, NatAs, 8, 577
Zhu, Z., Nelson, R. P., Dong, R., Espaillat, C., & Hartmann, L. 2012, ApJ, 755, 6
Zhu, Z., Nelson, R. P., Hartmann, L., Espaillat, C., & Calvet, N. 2011, ApJ, 729, 47